Review article **Open Access**

Deepak Thrithamarassery Gangadharan[a], Zhenhe Xu[a], Yanlong Liu, Ricardo Izquierdo and Dongling Ma*

Recent advancements in plasmon-enhanced promising third-generation solar cells

DOI 10.1515/nanoph-2016-0111
Received March 24, 2016; revised June 6, 2016; accepted June 9, 2016

Abstract: The unique optical properties possessed by plasmonic noble metal nanostructures in consequence of localized surface plasmon resonance (LSPR) are useful in diverse applications like photovoltaics, sensing, nonlinear optics, hydrogen generation, and photocatalytic pollutant degradation. The incorporation of plasmonic metal nanostructures into solar cells provides enhancement in light absorption and scattering cross-section (via LSPR), tunability of light absorption profile especially in the visible region of the solar spectrum, and more efficient charge carrier separation, hence maximizing the photovoltaic efficiency. This review discusses about the recent development of different plasmonic metal nanostructures, mainly based on Au or Ag, and their applications in promising third-generation solar cells such as dye-sensitized solar cells, quantum dot-based solar cells, and perovskite solar cells.

Keywords: plasmonic nanostructures; solar cells; thin films; localized surface plasmon resonance; photon management; light scattering-to-absorption ratio.

1 Introduction

The development and application of plasmonic metal colloidal solutions date back to the fourth century; at that time, people were largely fascinated by the beautiful color they possessed [1]. Scientific investigation of plasmonic nanoparticles (NPs) begun with Michael Faraday's seminal work on gold (Au) colloidal solution [2]. The brilliant color displayed by noble metal NPs is attributed to collective oscillation of conduction band electrons, known as surface plasmon resonance (SPR) [3, 4]. SPR can be turned over a wide spectral range from ultraviolet (UV), visible to near infrared (NIR) by adjusting the size and shape of plasmonic nanostructures. At resonances, photon absorption and scattering can be largely increased. The electromagnetic field in the proximity of plasmonic nanostructures can be significantly enhanced as well. Owing to their unique optical characteristics, nowadays, plasmonic metal nanostructures are used in a wide variety of applications ranging from sensing, optoelectronics to biological applications [5–8].

The sun continuously irradiates energy of 1.2×10^5 TW to earth, which is more than enough to satisfy the energy needs of humankind [9]. With this great hope, different solar energy conversion methods have been explored to meet our energy demand without incurring any negative impact to our environment. Photovoltaic (PV) cells, which can provide clean electrical energy by converting solar energy without any carbon costs associated with them, appear most promising [10]. Extensive researches are being carried out around the world to avail of cheap and efficient solar cells [11–13]. Another attractive method is converting solar energy to chemical energy by splitting water to produce hydrogen [14]. Hydrogen is a zero-emission, clean fuel, which has a potential to be employed in high power applications such as vehicles and aircrafts and to play a significant role in the so-called hydrogen economy [15, 16]. By employing plasmonic effects such as strong scattering, generation of hot electrons, and

[a]**Deepak Thrithamarassery Gangadharan and Zhenhe Xu:** These authors contributed equally to this work.
***Corresponding author: Dongling Ma,** Énergie, Matériaux et Télécommunications, Institut National de la Recherche Scientifique (INRS), 1650 Boulevard Lionel-Boulet, Varennes, Québec J3X 1S2, Canada, e-mail: ma@emt.inrs.ca
Deepak Thrithamarassery Gangadharan, Zhenhe Xu and Yanlong Liu: Énergie, Matériaux et Télécommunications, Institut National de la Recherche Scientifique (INRS), 1650 Boulevard Lionel-Boulet, Varennes, Québec J3X 1S2, Canada
Ricardo Izquierdo: Département d'Informatique, University of Quebec at Montreal (UQAM), Case postale 8888 succursale Centre-ville, Montréal, Québec, Canada

amplified near fields in PV devices and solar water splitting systems, photon harvest in the visible and near NIR regions of the solar spectrum can be greatly boosted in these applications. As a matter of fact, the introduction of plasmonic concepts into these applications has led to two emerging and recently rapidly growing research areas of plasmon-enhanced solar cells and plasmon-enhanced water splitting.

In this review article, we will present and discuss plasmonic metal nanostructure assisted solar energy conversion technologies, particularly plasmon-enhanced solar cells [17]. Third-generation solar cells such as dye-sensitized solar cells (DSCs), quantum dots (QDs)-based solar cells, and perovskite solar cells (PSCs) will be the focus of the discussion. We start with SPR fundamentals and major enhancement mechanisms reported in solar cells. Then the effect of the size, geometry, and concentration of the plasmonic nanostructures on solar cell performance is presented and discussed. Finally, we conclude this review with conclusions and perspectives of plasmon-enhanced solar cells.

2 SPR fundamentals and major enhancement mechanisms in plasmon-enhanced solar cells

In two different ways, plasmonic effects can be invoked in solar cells [18] (1) by the strong oscillation of conduction band electrons of metal NPs in phase with varying electric field of incident light known as localized surface plasmon resonance (LSPR) and (2) by surface plasmon polaritons (SPPs), which are surface electromagnetic waves that propagate along the metal-dielectric interface [19, 20]. The LSPR depends on geometry, size, and dielectric local environment of the metal NPs and magnifies itself by dramatically increased optical extinction and largely amplified local electromagnetic fields. The enhancement is maximum at a distance of ~3–6 nm and exponentially decreases within ~20–30-nm distance [21, 22]. SPPs originate via coupling of electromagnetic waves with electron plasma oscillations of the metal. Incident light can be trapped in the semiconductor absorber layer in a solar cell by converting it into SPPs at the metal-semiconductor interface. However, free space photons cannot excite SPPs due to the momentum mismatch between them. Therefore, a grating or prism is usually needed as coupling medium to satisfy the condition for the SPPs excitation [23]. Even though the penetration depth of SPPs is much higher (i.e. 100 nm–1 μm) compared to that of LSPR, the fabrication of corrugated metal back surface for SPP excitation is complex and expensive. On the contrary, the LSPR can be excited in solar cells simply by embedding pre-synthesized metal NPs in solar cells in most cases. In this review, our discussion is limited to the plasmon-enhanced solar cells using LSPR effects. LSPR can interact with the photoactive materials of solar cells via the strongly enhanced light absorption and scattering by plasmonic metal nanostructures at resonances and/or their large near fields. The exact of enhancement arising from these plasmonic effects largely depends on the size and geometry of metal NPs. Although in general, plasmonic NPs can improve the PV performance of the devices through enhancing light absorption of photoactive materials via increasing optical path length (far-field scattering) and light concentration (near-field antenna effect), parasitic absorption (i.e. an optical absorption process, which does not produce an electron-hole pair in the semiconductor and thereby not contributing to the photocurrent in the solar cell) by plasmonic metal nanostructures can have a negative impact. As such, plasmonic metal nanostructures exhibiting high scattering-to-absorption ratios are usually desired for solar cell applications.

2.1 SPR frequency

In thin film solar cells, strong local field enhancement around metal NPs can be used to increase light absorption of solar cells. The LSPR occurs when the frequency of electric field of incident light matches with the oscillation frequency of conduction band electrons in metal NPs (Figure 1). In this resonance situation, the oscillation of free electrons is enhanced considerably, producing a strong local electromagnetic field around the metal NPs [24]. This intense secondary electromagnetic field generated by the metal NPs can further excite nearly located

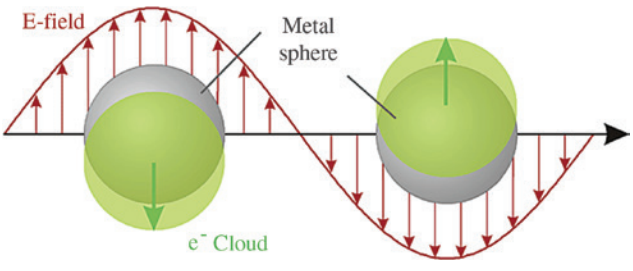

Figure 1: Schematic of plasmon oscillation for a sphere, showing the displacement of the conduction electron charge cloud relative to the nuclei. Reprinted with permission from [24]. Copyright 2003 American Chemical Society.

organic or direct band inorganic semiconductors to produce additional electron-hole pairs [25].

To understand enhanced light absorption by semiconductors via LSPR, we first briefly discuss the interaction of light with the metal particles [23]. Quasi-static approximation is used to analyze interaction of electromagnetic waves with particles that have the size less than that of the incident wavelength (λ). This approximation is only valid when particle size (d) is well below 100 nm in diameter (i.e. $d<<\lambda$) [21]. This condition allows us to treat the problem as an electrostatic field over a spherical particle, as the harmonically oscillating electromagnetic field is constant over the particle volume.

To calculate electric potentials (inside and outside of the spherical particle) and thereby electric fields of a sphere with radius 'a', it is usually assumed that the sphere is situated in a uniform static electric field of $E=E_0\hat{z}$, where $\hat{z}$ is a unit vector in z direction and surrounded by isotropic and non-absorbing medium with a dielectric constant ε_m. The potentials can be obtained by solving the Laplace equation $\nabla^2\Phi=0$, where Φ is the electric potential. The rigorous mathematical derivation is out of the scope of this review, and there are some excellent textbooks and articles are available for reference [26, 27]. Considering the azimuthal symmetry of the problem and applying boundary conditions, electric potential inside and outside of the sphere can be obtained [26]. Briefly, it was found that the potential outside the sphere corresponds to the superposition of the applied electric field and that of the dipole located at the particle center.

The applied field induces a dipole moment $\vec{p}$ inside the sphere, which can be defined as follows:

$$\vec{p}=4\pi\varepsilon_0\varepsilon_m a^3\frac{\varepsilon-\varepsilon_m}{\varepsilon+2\varepsilon_m}E_0, \tag{1}$$

where ε_0 is permittivity of vacuum. We can write the expression for polarizability (α) from the above equation by using $\vec{p}=\alpha\varepsilon_0\varepsilon_m E_0$. Therefore, polarizability can be defined by the equation below:

$$\alpha=4\pi a^3\frac{\varepsilon-\varepsilon_m}{\varepsilon+2\varepsilon_m}, \tag{2}$$

where ε is the dielectric response of the metal sphere.

When $|\varepsilon+2\varepsilon_m|$ becomes a minimum, i.e. when Re $\{\varepsilon(\omega)\}=-2\varepsilon_m$, the polarizability experiences resonant enhancement. According to Drude's model for metals, dielectric response of the metal sphere $\varepsilon(\omega)$ is a complex number and real component of dielectric response can be correlated with frequency by the following expression:

$$\text{Re}\{\varepsilon(\omega)\}=1-\frac{\omega_p^2}{\omega^2+\gamma^2}, \tag{3}$$

where ω is the frequency of electric field and $\gamma=1/\tau$ and τ is the relaxation time of the electron. ω_p is the plasma frequency (ω_p) of the free electron gas in a metal, which is defined as follows:

$$\omega_p=\sqrt{\frac{n_e e^2}{\varepsilon_0 m e^*}}, \tag{4}$$

where n_e is the electron number density, e is the electric charge, and m_e^* is the effective mass of the electron.

From equation (3) and resonance condition (i.e. Re $\{\varepsilon(\omega)\}=-2\varepsilon_m$), the expression for SPR frequency (ω_{LSPR}) can be derived [23] as follows:

$$\omega_{\text{LSPR}}=\omega_p\sqrt{\frac{1}{1+2\varepsilon_m}-\frac{1}{\omega_p^2\tau^2}}, \tag{5}$$

where ω_p is defined by equation (4). It can be immediately seen from this relationship that plasmonic resonant frequency strongly depends on the dielectric environment. For most of the noble metals, ω_p lies in the deep ultra violet region. It should be noted that, as the resonant frequency of plasmonic metal NPs red shifts as ε_m increases and as in the solar cell applications, plasmonic metal NPs are usually embedded in a high dielectric environment like silicon, TiO_2, ZnO, and PbS; the red shifting of their resonance wavelength is expected and has been often exploited in solar cells to extend light absorption to longer wavelengths of the solar spectrum.

2.2 Near-field antenna effect

At resonance, SPR is accompanied by strong near fields due to resonant enhancement in polarizability. The electric field inside (E_{in}) and outside (E_{out}) of the NP can be further deduced from the potentials obtained using the Laplace equation [23] and described by the following:

$$E_{\text{in}}=\frac{3\varepsilon_m}{\varepsilon+2\varepsilon_m}E_0, \tag{6}$$

$$E_{\text{out}}=E_0+\frac{3\hat{n}(\hat{n}\cdot\vec{p})-\vec{p}}{4\pi\varepsilon_0\varepsilon_m}\frac{1}{r^3}, \tag{7}$$

where $\hat{n}$ is the unit vector and r is the distance to the center of the spherical NP.

On the right hand side of equation (7), the first term represents the incident electric field and the second term represents the induced electric field by the dipole inside the spherical particle. The maximum field-enhancement occurs at the resonance condition in consequence of polarizability attaining the maximum value. The exact level of near field enhancement that plasmonic nanostructures can achieve near their surface is affected by their morphology, which also determines the near field distribution surrounding them. In Figure 2, three-dimensional full-wave finite-difference time-domain (3D FDTD) stimulations show near-field distribution of different shaped Au nanostructures [28, 29]. For instance, plasmonic nanostructures with sharp tips produce larger field enhancement. In Au nanocubes, intense near field enhancement has been reported at corners and edges [30]. As the electron-hole generation rate of semiconductors is related to the intensity of the electric field as $|E|^2$, such near-field enhancement can increase the generation rate of electrons and holes by several orders of magnitude [22, 31]. It should be noted that the dipole contribution quickly falls down $\left(\propto\frac{1}{r^3}\right)$ when moving away from the particle (Figure 3). The expression for the electric field outside

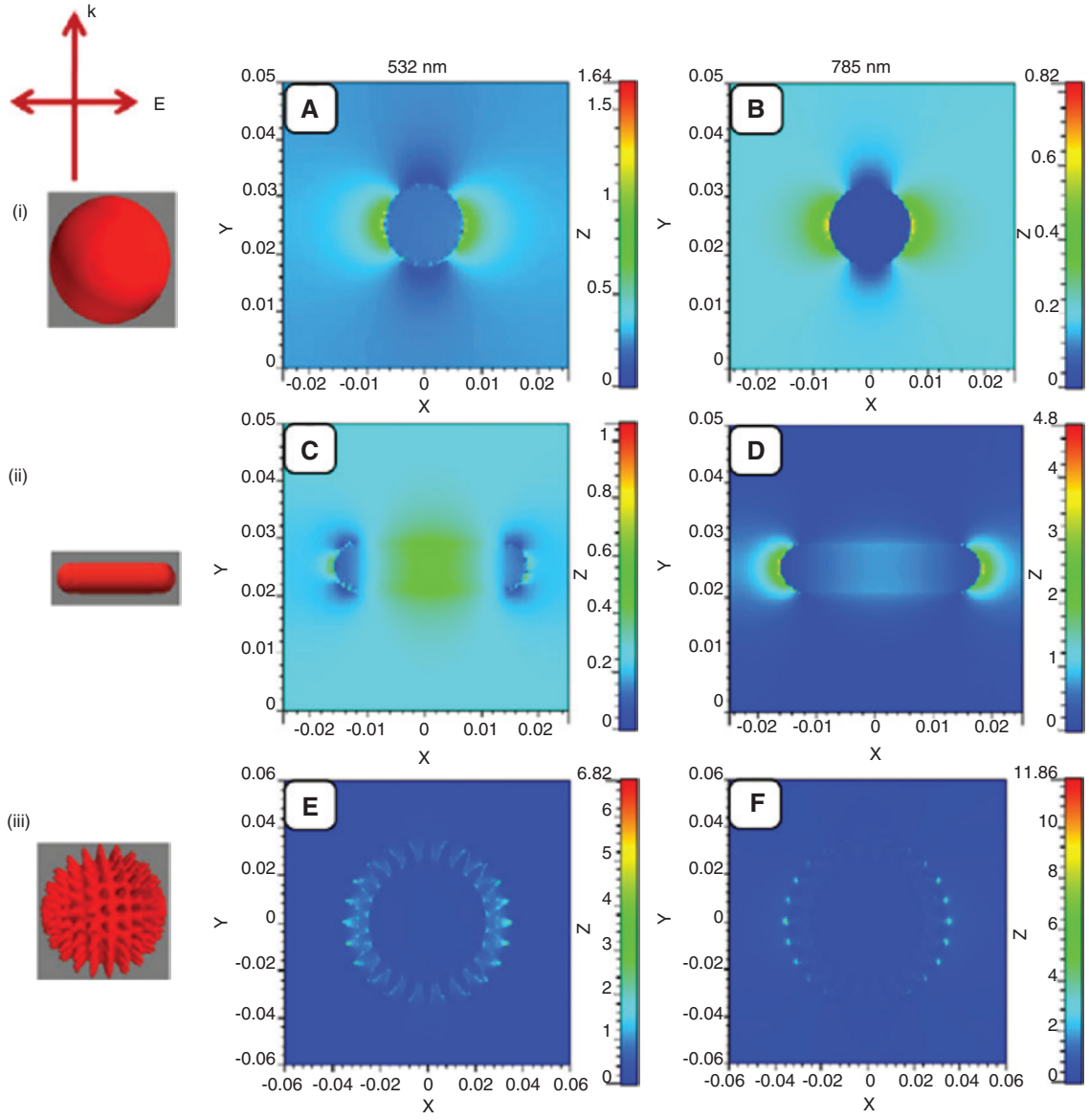

Figure 2: 3D FDTD simulated electromagnetic field distributions of a gold (i) nanosphere, (ii) nanorod, and (iii) nanostar under excitations of [(A), (C), (E)] 532-nm and [(B), (D), (F)] 785-nm lasers. The intensity scale is normalized as $E=E_0$. Reprinted with permission from [28]. "© IOP Publishing. Reproduced with permission. All rights reserved".

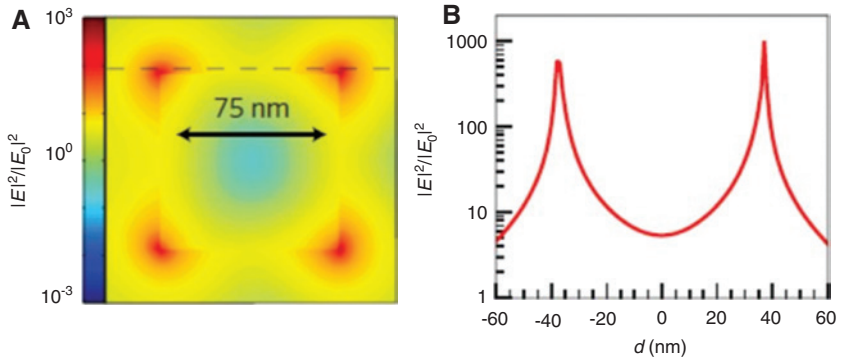

Figure 3: (A) Spatial distribution of the SPR-induced enhancement of electric field intensity at the SPR peak wavelength (420 nm), from a FDTD simulation of a 75-nm Ag nanocube. (B) Enhancement in the electric field intensity at the SPR peak wavelength as a function of distance, *d*, along the dashed line. Reprinted by permission from Macmillan Publishers Ltd. Nature Materials [22], copyright 2011.

the NP clearly suggests that, to utilize the near-field effects efficiently in solar cells, metal NP-semiconductor spacing should be as low as only few nanometers [32].

2.3 Far-field scattering effect

The light scattering induced by plasmonic resonance can be used to trap the light inside solar cells, which increases the optical path length through the solar cell absorber layer and thereby its photocurrent [33, 34].

The absorption and scattering cross-sections of a sphere can be calculated by using Poynting-vector [35].

$$C_{abs}=k\ \mathrm{Im}[\alpha]=4\pi k\ a^3\ \mathrm{Im}\left[\frac{\varepsilon-\varepsilon_m}{\varepsilon+2\varepsilon_m}\right], \tag{8}$$

$$C_{sca}=\frac{k^4}{6\pi}|\alpha|^2=\frac{8\pi}{3}k^4\ a^6\left|\frac{\varepsilon-\varepsilon_m}{\varepsilon+2\varepsilon_m}\right|^2, \tag{9}$$

where $k=2\pi/\lambda$ and λ is the wavelength of incident photon.

The above equations show that both absorption and scattering cross-sections are enhanced when plasmonic resonance condition is satisfied ($\mathrm{Re}\{\varepsilon(\omega)\}=-2\varepsilon_m$). The light scattering cross-section is more rapidly enhanced with the size compared with the absorption cross-section, as the former scales as a^6, whereas the latter, a^3. In order to take advantage of the plasmonic effects (here considerably enhanced optical path) yet avoid too much parasitic absorption reducing the optical absorption by the semiconductor, relatively larger particles that yield larger scattering-to-absorption ratios (C_{sca}/C_{abs}) are preferred. The relationship between NP size and C_{sca}/C_{abs} is plotted in the graph (Figure 4) [36]. This may also be achieved by synthesizing plasmonic metal nanostructures of different morphologies, as the ratio is also sensitive to the morphology of metal nanostructures.

3 Plasmon-enhanced third generation solar cells

Silicon has dominated the PV market for the past few decades [37]. The cost of PV modules still has to be significantly reduced for making solar cells, an affordable and large scale implemented technology [38]. The most recently proposed third-generation thin film solar cells target at both low cost and high efficiency. They are so far the best option for the cost-effective PV technology because of their low material and processing cost [39, 40].

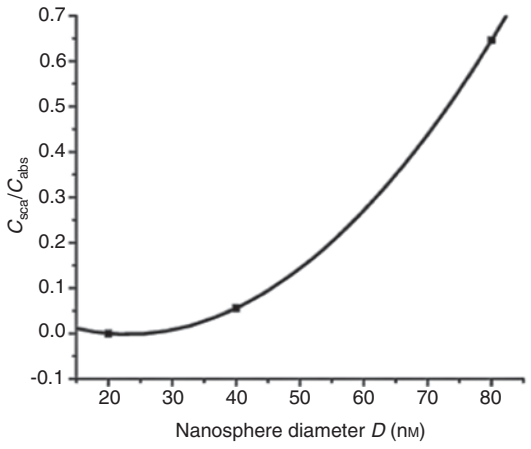

Figure 4: Tunability of the ratio of scattering to absorption of nanoparticles. Variation of C_{sca}/C_{abs} with nanosphere diameter *D*. Reprinted with permission from [36]. Copyright 2006 American Chemical Society.

Unfortunately, in addition to long-term stability issue, their efficiencies are still lower as compared to those of silicon wafer solar cells mainly because of insufficient light absorption across the entire solar spectrum. Improving light absorption thus represents a critical and promising solution. There are a number of ways to improve optical absorption of solar cells, such as using antireflection coatings, texturing substrate surfaces, involving plasmonic metal nanostructures, etc. [41, 42]. Optical absorption and photocurrent have been found to be significantly improved with the integration of plasmonic metal nanostructures. Compared with other strategies, this approach is advantageous because the optical feature of plasmonic metal nanostructures (and thereby absorption enhancement) can be easily tuned by varying their size and shape through low cost, wet chemical methods and because of ease of fabrication of plasmon-enhanced solar cells in most cases as well [11].

In this review, we intentionally choose three types of promising solar cells, namely, DSCs, QD bulk heterojunction (BHJ) solar cells, and hybrid inorganic-organic PSCs to discuss about plasmon-enhanced solar cells. DSCs are so far the most intensely researched third-generation solar cells [12]. Comprehensive knowledge achieved on plasmon-enhanced DSCs will be quite useful for exploring the plasmonic effects of metallic NPs in other emerging PV devices like PSCs that share similar operating mechanisms. Among the different types of QDs-based solar cells, QD BHJ solar cells are superior in providing stable and good PV performance, so plasmonic effects in QD BHJ solar cells will also be discussed in this review [13].

3.1 Dye-sensitized solar cells

DSCs have attracted tremendous research interest from researchers working in academia and industry due to their capability to replace expensive silicon PV technology [43]. Typical DSCs consist of a mesoporous semiconductor oxide film (for example, TiO_2) sensitized with a molecular type dye, sandwiched between a conductive glass substrate and a platinum (Pt)-coated counter electrode with a redox shuttle (electrolyte) in between the electrodes for dye regeneration [12]. Despite the intense research on various aspects from dye molecule and electrolyte design to the morphology innovation of metal oxide film, the best overall power conversion efficiency (PCE) (~13%) of DSCs is still much lower than that of silicon solar cells [44]. The incorporation of plasmonic metal NPs into DSCs appears to be a highly promising, alternative strategy for further PCE improvement, and it has been well investigated over the past several years in the field of DSCs.

Moreover, the thinning of the photoanode (semiconductor metal oxide) film can also be realized by plasmon-enhanced DSCs without sacrificing PV performance. By thinning the solar cells, in addition to the reduction of material costs, photovoltage can be improved by decreasing the surface area of the semiconductor oxide. A dramatic improvement in PCE of about 84% (PCE: ~10%) was reported with a remarkably thinner TiO_2 film (about 4 μm vs. 12 μm typically used) in DSCs with the help of plasmonic NPs [45]. This efficiency is comparable to the highest efficiency achieved by conventional DSCs with a thick TiO_2 film.

In constructing plasmon-enhanced DSCs, several important factors have to be taken into consideration and are described below.

3.1.1 Geometric position of metal NPs in DSCs

Hou et al. investigated three different geometric configurations of metal NPs/dye/TiO_2 in the photoanode of plasmonic DSCs [46]: (1) metal NPs embedded TiO_2 film sensitized with dye, (2) metal NPs deposited on the top of bare TiO_2 layer and sensitized with dye, and (3) metal NPs deposited on the top of dye-sensitized TiO_2 film. Figure 5 shows three different configurations and their PV performance. The short-circuit photocurrent of differently configured working electrodes was measured with 28-s laser exposure at wavelength of 532 nm. The highest short-circuit photocurrent was obtained for the first configuration followed by the third and second configurations. The overall PCE improved by about 57% for the working electrode where Au NPs were embedded inside the TiO_2 film as compared to pristine TiO_2 electrode. In this study, deposition of Au NPs on the top of TiO_2 film showed a decrease in efficiency. In another study, plasmonic effects were invoked via depositing silver (Ag) NPs in between two TiO_2 layers in the photoanode [47]. Even though the photocurrent was enhanced by 23%, the fill factor (FF) was significantly reduced. A similar kind of configurations, i.e. plasmonic nanostructures placed at two interfaces of TiO_2 layers (i.e. the interface of compact TiO_2 layer/transparent active layer and the interface of transparent active layer/scattering layer) yielded 34% photocurrent enhancement [48]. However, embedding metal NPs inside the metal oxide film is usually less complicated and thus a widely adopted strategy in DSCs [49, 50].

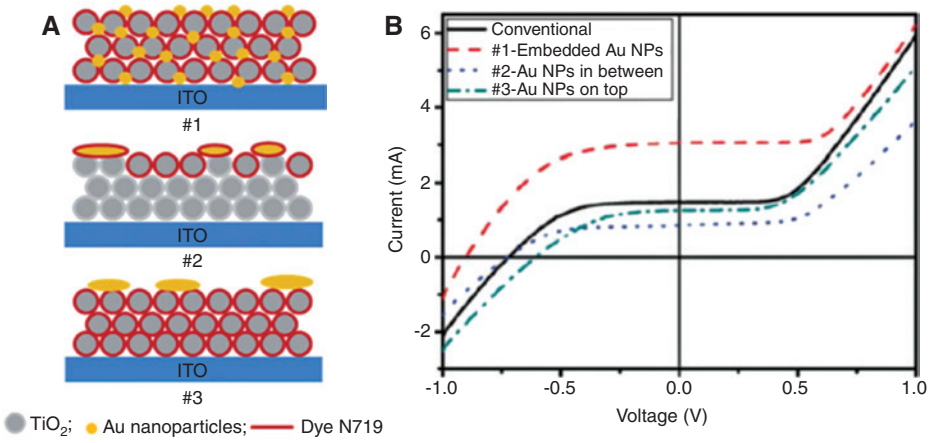

Figure 5: (A) Schematic diagrams of three different Au nanoparticle/dye/TiO_2 configurations, (B) I–V characteristics of DSCs with different working electrodes. Reproduced from [46] with permission of The Royal Society of Chemistry.

3.1.2 Effect of size and concentration of metal NPs on the performance of DSCs

As we discussed in the previous section, the volume of a single NP is directly proportional to its extinction cross-section and its scattering-to-absorption ratio. Spherical metal NPs sized between 5 and 100 nm have been commonly used in DSCs. Light absorption dominates when NPs' size is below 40 nm. As the particle size increases, light scattering enhances significantly, which is beneficial in enhancing the photocurrent [36, 51]. When particle size was larger than 80 nm, broadening of their extinction spectrum and redshift was also observed (Figure 6) [52]. The metal NPs with their diameter between 35 and 45 nm are highly recommended in DSCs for enhancing the photocurrent without compromising on dye loading [32]. These intermediately sized NPs can also produce an intense localized field (near-field), which overlaps with the absorption peak of commonly used dyes. This near-field effect enhances the photocurrent in DSCs by increased dye excitation [12, 44, 53].

The size of metal NPs also influences the open-circuit voltage (V_{oc}) of plasmon-enhanced DSCs due to photocharging effect [54]. The storing of photoexcited electrons within the metal NPs is known as photocharging, which can cause a shift in quasi-Fermi level of metal/semiconductor composites, as first proposed by Subramanian's group [55]. Figure 7A shows Fermi level equilibrium in a semiconductor-metal nanocomposite through photocharging. A negative shift in flat band potential [from −0.98 V to −1.14 V vs. saturated calomel electrode (SCE)] was observed for the TiO_2 electrode embedded with 5-nm-sized Au NPs compared to pristine TiO_2 electrode (Figure 7B). In plasmonic DSCs, a negative shift in

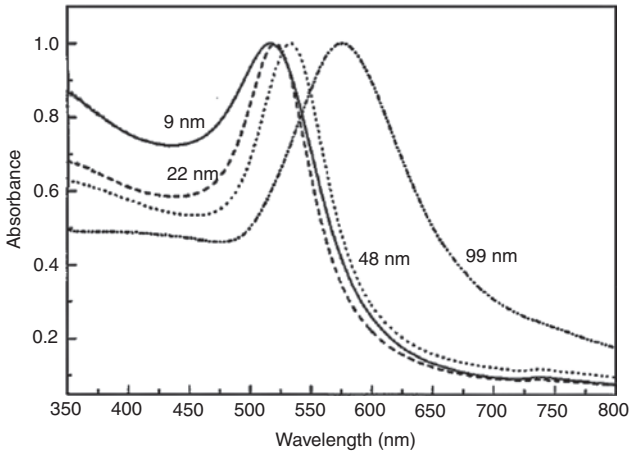

Figure 6: UV-vis absorption spectra of 9-, 22-, 48-, and 99-nm gold nanoparticles in water. All spectra are normalized at their absorption maxima, which are 517, 521, 533, and 575 nm, respectively. Reprinted with permission from [52]. Copyright 1999 American Chemical Society.

quasi-Fermi level of electrode resulted in the enhancement of V_{oc} in DSCs [46, 47, 56]. Li et al. observed an increment in V_{oc} by 131 mV when they incorporated 2-nm-sized Au NPs in the photoanode [45]. The authors obtained the best overall PCE of about 10.1% with 0.168 wt% of Au NPs in TiO_2 film. At a higher concentration of 0.8 wt%, the V_{oc} shot up to 897 mV, which is close to the theoretical maximum (~950 mV) [57]. Wang et al. investigated the relationship between V_{oc} and size of metal NPs in the photoanode [54]. The current density was higher for DSCs with 45-nm metal NPs than those with 5-nm metal NPs, but the latter showed a higher overall PCE (Figure 7C). Electrochemical impedance spectroscopy (EIS) measurements revealed that recombination resistance (R_{ct}, i.e. resistance against electron recombination) and electron effective lifetime

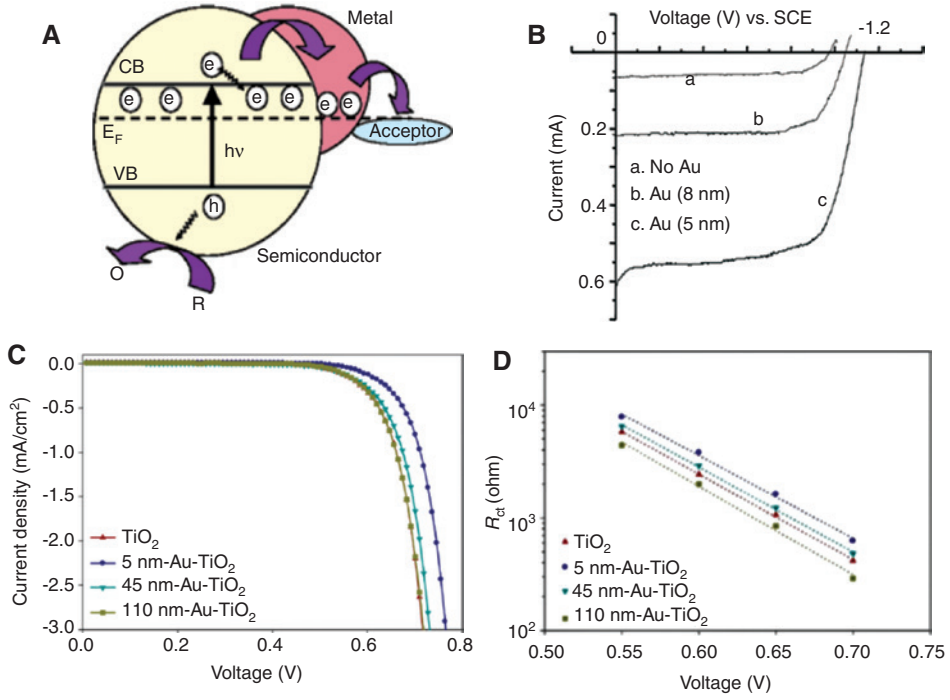

Figure 7: (A) Fermi level equilibration in a semiconductor-metal nanocomposite system, (B) I–V characteristics of (a) TiO_2, (b) TiO_2/Au (8-nm diameter), and (c) TiO_2/Au (5-nm diameter) composite film. Measurements were performed in a three-arm cell with Pt as counter electrode, an SCE as reference, and 3-mL 0.05 M NaOH as electrolyte. UV light from Xenon lamp (λ>300 nm) was used as the excitation source. Reprinted (adapted) with permission from [55]. Copyright 2004 American Chemical Society. (C) *J–V* curves of Au–TiO_2 DSSCs and TiO2-DSSCs under AM-1.5G one sun irradiation. (D) Recombination resistance (R_{ct}) at TiO_2/electrolyte interfaces as a function of applied forward bias. Reproduced from [54] with permission of The Royal Society of Chemistry.

decreased as the particle size was increased (Figure 7D). The DSC with 5-nm metal NPs exhibited the highest R_{ct} (i.e. the lowest electron recombination). Dark current was also considerably lowered for the DSCs with smaller NPs due to the photocharging effect.

Another important parameter in determining the PCE is concentration of metal NPs added to the semiconductor oxide film. In general, lower concentrations of spherical metal NPs (ranging from 0.1 wt% to 0.2 wt%) in photoanodes resulted in the largest enhancement in photocurrent and overall PCE. The incident photon-to-current efficiency (IPCE) measurement of the photoanode (Figure 8) shows that photocurrent was significantly reduced when the concentration of spherical metal NPs was above 0.168 wt% in the photoanode [45]. The reduction in photocurrent at higher concentration of metal NPs in DSCs is mainly due to the reduction in dye loading and inefficient electron injection from dye to semiconductor metal oxide. There are contradictory reports about dye loading, but most of the studies show that dye loading on the photoanode reduces as the concentration of metal NPs is increased [58]. At higher metal NP concentrations, a negative shift of the conduction band of metal oxide

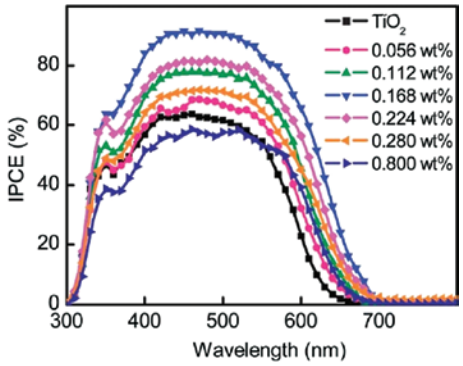

Figure 8: IPCE spectra of the DSCs based on FNE29 sensitized pure TiO_2, or Au–TiO_2 (Au–TiO_2 0.056, 0.112, 0.168, 0.224, 0.280, and 0.800 wt%) films. Reproduced from [45] with permission of The Royal Society of Chemistry.

reduces the driving force for the transfer of photoexcited electrons from the dye to the metal oxide resulting in less efficient electron injection. In the case of anisotropic metal NPs, the optimum concentration of metal NPs for the best PV performance was found to be much higher than 0.2 wt% and to depend on the specific shape of the anisotropic metal NPs [59].

The distance between metal NPs and nearby dye molecules is critical in plasmon-enhanced DSCs. Largest near-field enhancements in DSCs was obtained when the distance was as short as 2 nm [60]. The redshift in absorption wavelength was also observed when the distance was increased [61].

3.1.3 Morphology of metal NPs in DSCs

3.1.3.1 Spherical metal NPs

In early studies on plasmon-enhanced DSCs, researchers mainly used spherical noble metal (Au, Ag, etc.) NPs to enhance the photocurrent. In one of the first investigations on plasmon-enhanced DSCs, Zhao et al. prepared the TiO_2-Au/Ag composite by sol-gel method [62]. There are also reports on incorporation of metal NPs by thermal evaporation [63]. The performance and stability of these devices were poor due to lack of finely controlled synthesis and fabrication.

The rapid development in synthetic chemistry in recent years allows researchers to tune metal NPs precisely for the specific needs of particular applications. Li et al. synthesized, with a good control, a nanocomposite of Au NPs directly inlaid in TiO_2 matrix and used it as the photoanode film of DSCs [45]. Such DSCs involving 0.168 wt% of Au NPs showed significant improvement in efficiency by 84%, photovoltage by 97 mV, and photocurrent by 64%. It is worth mentioning that these authors achieved a high PCE of 10.1% for a very thin (~4 μm) photoanode film. In this work, the authors chose metal-free organic dye sensitizer, FNE29, over widely used N719 to provide a higher driving force for electron injection from the lowest unoccupied molecular orbital (LUMO) of the dye to TiO_2 conduction band, as the LUMO of FNE29 is 0.27 V more negative than that of N719. The absorption peak of FNE29 and the LSPR band of 2-nm Au NPs also overlap well, which is advantageous for efficiently improving the optical absorption of the solar cells. The Au NPs inlaid TiO_2 nanocomposite was synthesized by using cross-linked polymerized ionic liquid (CLP) [64]. Briefly, sodium borohydride ($NaBH_4$)-methanol mixture was added into chloroauric acid ($HAuCl_4$) dissolved with CLP-methanol mixture to synthesize 2 nm Au NPs. The CLP capped Au NPs and TiO_2 paste were then blended to obtain the nanocomposite for the photoanode film. The photoanode was sintered at 500°C to decompose the CLP and obtain Au NPs inlaid TiO_2 nanocomposite. Here, "cross-linked polymerized ionic liquid" played an important role in fixing Au NPs on the surface of TiO_2 by electrostatic effect. In this particular nanocomposite, polymer stabilizer around Au NPs provided thermal and structural stability in the process of high temperature sintering of the photoanode. In addition to improvement in photocurrent by the near-field effect, the V_{oc} enhancement due to negative shift of quasi-Fermi level significantly contributed in a large enhancement of PCE.

There were also several efforts to decorate one-dimensional semiconductor oxide nanostructures with metal NPs [50, 65]. Generally speaking, the long-term stability has been a great concern for the plasmon-enhanced DSCs because most commonly used iodide/triiodide electrolyte in DSCs can easily destroy the metal NPs [66]. One immediate way to achieve stable plasmon-enhanced DSCs is to replace this corrosive electrolyte with one containing non-corrosive redox mediator. Cobalt-based electrolytes are proved to be a good alternative to provide long-term stability for the plasmon-enhanced DSCs [67]. But the efficiency of the plasmon-enhanced DSCs using cobalt (II/III) tris (2, 2′-bipyridine) ([Co (bpy) 3]$^{2+/3+}$) redox mediator has to be largely improved by further optimization.

3.1.3.2 Core-shell nanostructures

In earlier reports, plasmonically enhanced DSCs were instable because the highly reactive iodine/triiodide electrolyte could corrode metal NPs [68, 69]. For example, Au NPs can easily dissolve in I^-/I_3^-as given below:

$$2Au + I_{3^-} + I^- \leftrightarrow 2\left[AuI_2\right]^-.$$

Another major concern associated with metal NPs is that they can act as electron recombination centers in solar cells. To avoid the aforementioned issues, protecting core metal NPs with an insulating layer or shell, known as core@shell nanostructures, has been widely adopted [38, 52, 66]. In these core@shell nanostructures, wide bandgap materials (mainly SiO_2 and TiO_2) are used as shell materials around the metal core. The SPR peak wavelength and intensity of the core@shell nanostructure depend on the shell thickness, so controlling shell thickness is very essential (Figure 9) [70].

The choice of the shell material also influences the PV performance parameters in plasmon-enhanced DSCs. If the shell of the metal NPs can inject electrons to them, the apparent Fermi level shifts negatively, which leads to the photocharging effect and increase of V_{oc} [71]. This was exactly the case when TiO_2, which can transfer photoexcited electrons, was used as a shell material (Figure 10) [56]. Quite different results were obtained when SiO_2 that does not have any charge transfer behavior with metal NPs was used as a shell material, where V_{oc} remained unchanged.

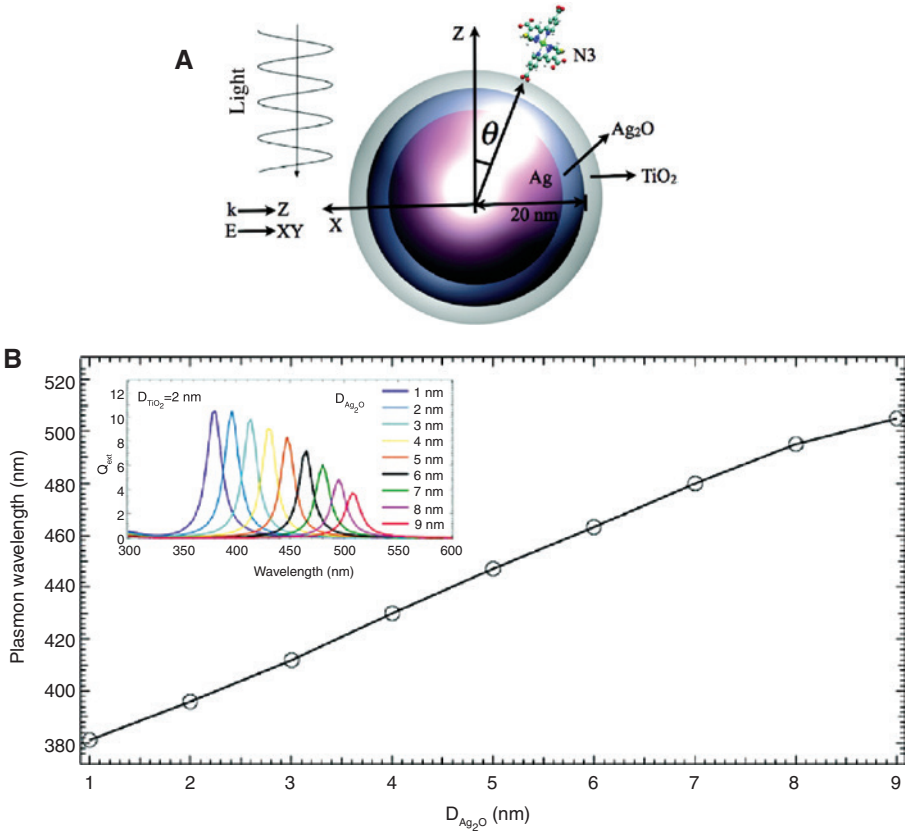

Figure 9: (A) Structure of the N3/TiO_2/Ag composite DSSC, where the incident light propagates along axis *Z*, and the polarization direction is uniformly distributed in the *XY* plane. The relative location of N3 dye on the TiO_2 surface is indicated by the polar angle, θ and (B) dependence of plasmon wavelength on the thickness of Ag_2O (D_{Ag_2O}) when the thickness of TiO_2 (D_{TiO_2}) is fixed at 2.0 nm, and the radius of the oxidized silver sphere ($R_{Ag}+D_{Ag_2O}$) is fixed at 20.0 nm. The results from FDTD simulation and Mie theory are presented in red and black lines, respectively. In addition, the extinction profile as a function of D_{Ag_2O}, which is calculated from Mie theory, is illustrated in the inset. Reprinted with permission from [70]. Copyright 2004 American Chemical Society.

Instead, the photocurrent was improved simply due to the near-field effect. Figure 10A shows these two different scenarios regarding the effect of the shell material.

Brown et al. also investigated the plasmonic effect of Au@SiO_2 core@shell nanostructures in DSC applications [72]. They employed Au@SiO_2 in both solid-state and liquid electrolyte DSCs to enhance their absorption in the visible region of the spectrum. The Au NPs were first synthesized by a widely adopted Turkevich method [73, 74]. Then the Stöber method was used to grow silica around Au cores [75]. It is worthwhile to emphasize that the reproducibility of silica coating using Stöber method depends on several synthesis parameters like pH, temperature, and chemical purity [76–78], and in particular, for getting a thin silica shell in a controlled fashion, a modified Stöber method has to be often used [73, 79]. In this approach, citrate capping ligands of the Au NPs were replaced by silane linker molecules (typically aminosilanes or mercaptosilanes), which then act as excellent reaction sites for the silica growth [80].

Brown et al. observed the decrease in both FF and V_{oc} when they incorporated bare Au NPs into solid-state and liquid electrolyte based DSCs due to enhanced charge carrier recombination on the surface of metal NPs. To avoid or minimize this negative effect, a silica shell was introduced. It was found that in addition to chemical and electrical insulation, the shell also provided thermal stability to the metal core. The photoanode film sintering at 500°C is essential for good adhesion and crystallinity of the semiconductor oxide film on the glass substrate. Upon heat treatment, the bare Au NPs in TiO_2 film underwent size enlargement, resulting in a redshift in the absorption [51]. As a result, the SPR band of bare Au NPs after heat treatment separated from the absorption peak of dye, and the dyed film thus showed two distinctive absorption peaks, which corresponded to dye and Au NPs, respectively (Figure 11A). In clear contrast, the dyed film containing Au@SiO_2 core@shell NPs still exhibited a single absorption peak at 525 nm even after sintering,

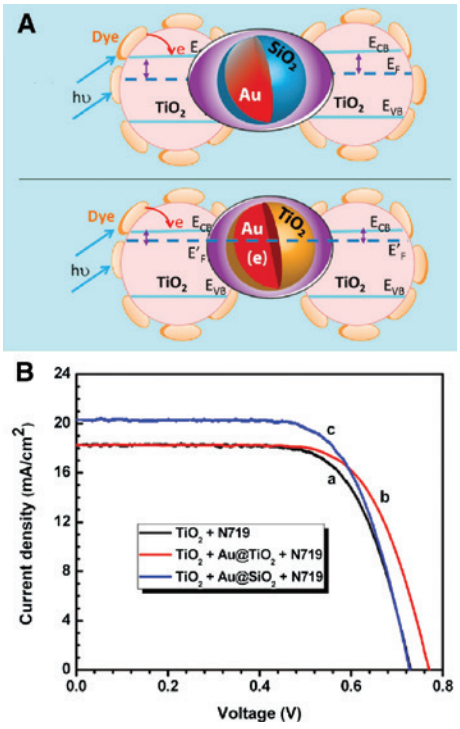

Figure 10: (A) Electron equilibration and its influence on the apparent Fermi level (E_F): dye-TiO_2/Au@SiO_2, and dye-TiO_2/Au@TiO_2, (B) *J*–*V* characteristics of DSCs with TiO_2/Au@SiO_2 and TiO_2/Au@TiO_2. Reprinted with permission from [56]. Copyright 2012 American Chemical Society.

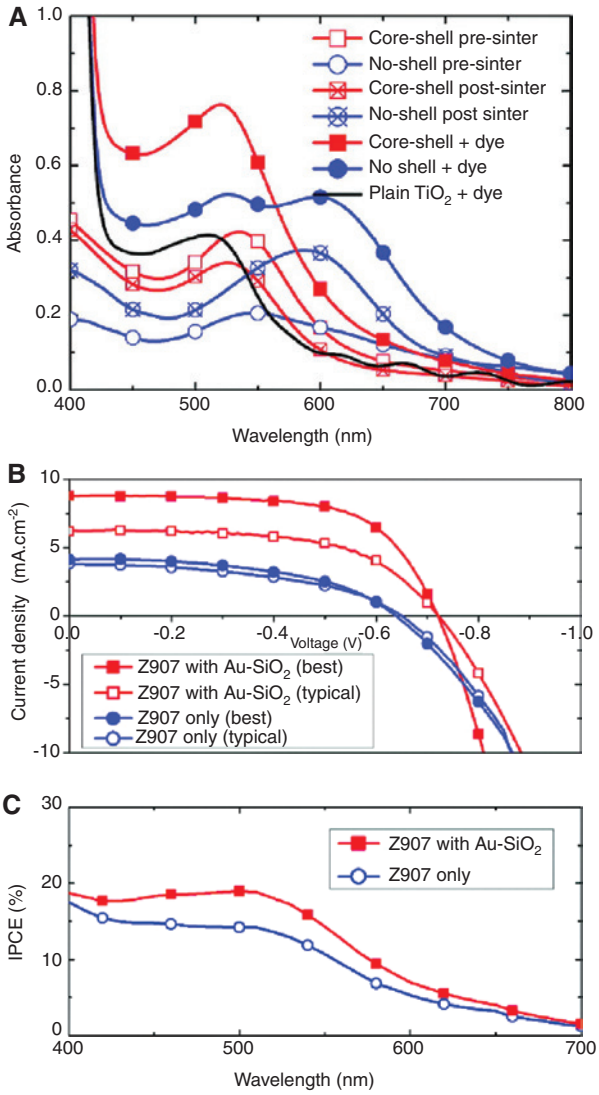

Figure 11: (A) Absorption spectra of thin films (~1 μm) processed with conventional mesoporous TiO_2 paste at different stages in the fabrication process; directly after doctor blade coating (open symbols, "pre-sinter"), after two thermal sintering cycles at 500°C and a chemical $TiCl_4$ treatment (open symbols with cross-through, "post-sinter"), and with final dye-sensitization with Z907 ruthenium complex (solid symbols). (B) Current density voltage curves measured under simulated AM1.5 sun light at 100 mWcm^{-2} for devices with Z907 dye-only and combined Au-SiO_2 and Z907 sensitization. (C) Incident photon-to-electron conversion efficiency (IPCE) spectra for a typical Z907 dye-only sample and a sample with the additional coating of Au-SiO_2 nanoparticles after dye-sensitization, but prior to hole-transporter coating. The curves for both a typical and the best device from the series are shown for both systems. Reprinted with permission from [72]. Copyright 2011 American Chemical Society.

resembling the initial SPR band of Au@SiO_2 NPs and overlapping the absorption maxima of dye, strongly suggesting that the Au cores were not altered during the sintering treatments. This effect could be more straightforwardly observed in Figure 12, where silica-coated Pt NPs displayed no noticeable change in their size following the heat treatment at 550°C [81]. Thanks to the presence of these stable Au@SiO_2 NPs, the photocurrent, FF and V_{oc} were all improved in Au@SiO_2 incorporated solid-state DSCs with respect to corresponding Au-free DSCs (Figure 11B and C). No significant change in solar cell performance was observed when the thickness of silica shell was varied from 3 to 8 nm, which agrees with Standridge et al.'s study on the shell thickness [60]. In another study, the optimum thickness of the shell in core@shell nanostructures was found to be 5 nm for the DSC application [82].

Qi et al. incorporated Ag@TiO_2 core@shell NPs into photoanodes, resulting in ~30% of PCE enhancement [71]. Here, the authors adopted a modified polyol process to synthesize Ag NPs. Briefly silver nitrate was added to ethylene glycol containing poly (vinylpyrrolidone) (PVP) and the mixture was stirred until the complete dissolution of silver nitrate. The mixture solution was subsequently heated for the formation of Ag NPs, followed by the introduction of titanium isopropoxide for achieving a 2-nm-thick shell of TiO_2 around Ag NPs.

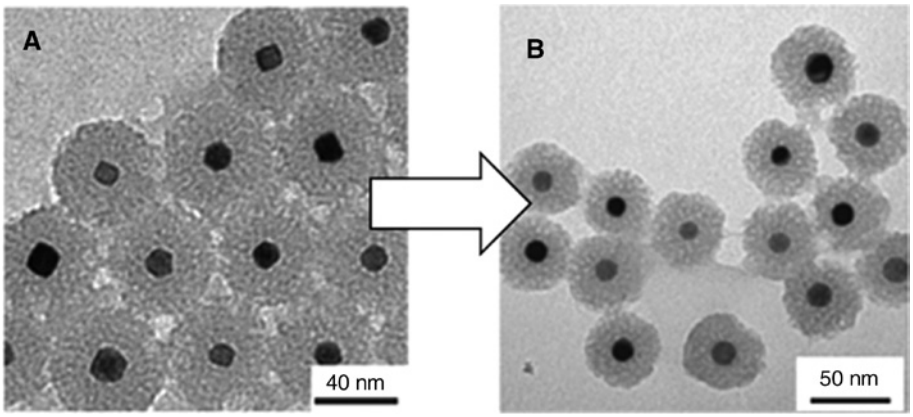

Figure 12: TEM images (A) as-synthesized Pt@SiO_2 nanoparticles and (B) Pt@SiO_2 nanoparticles after calcination at 550°C. Reprinted by permission from Macmillan Publishers Ltd. Nature Materials [81], copyright 2009.

To achieve broadband light harvesting in DSCs, use of multiple-shell core@shell structures has also been investigated [83]. The multiple-shell nanostructures consisting of a TiO_2 NP as a single core and subsequent Au and TiO_2 shells (denoted as TAuT) showed tunable LSPR wavelength (λ_{LSPR}) in visible-near-infrared (vis-NIR) (Figure 13). The λ_{LSPR} could be tuned by varying the thickness of the intermediate shell of Au. For synthesizing TAuT, the authors first modified the surface of the TiO_2 NP via layer-by-layer coating of polyelectrolytes [84–87]. Aqueous solution of modified TiO_2 NPs was then mixed with $HAuCl_4$ solution. Surface confined growth of the Au shell was initiated by adding 5% hydroxylamine-containing aqueous solution. Furthermore, Au shell encapsulated TiO_2 NPs were treated with titanium butoxide in ethanol to obtain the external shell of TiO_2. With the use of these TAuT NPs in DSCs, the light harvesting was particularly improved in the NIR region of the solar spectrum, where the light absorption by the N719 dye is weak. The IPCE spectra clearly show photocurrent enhancement in the wavelength range of 550–750 nm (Figure 14). The core@shell nanostructures consisting of multiple shells around the plasmonic metal NP core have also been explored to take advantages of both SiO_2 and TiO_2 shells [66, 70]. In the metal NPs@SiO_2 core@shell nanostructure, even though the SiO_2 shell provides electrical and chemical insulation to metal NPs compared with TiO_2, resultant performance has been limited by ineffective dye loading and inefficient electron injection to SiO_2.

Au@TiO_2 hollow submicrospheres were also utilized in DSCs, which could enhance the PCE by 30% compared with conventional DSCs (Figure 15A) [88]. The microspheres were synthesized by the controlled hydrolysis of titanium tetrafluoride (TiF_4) in Au NPs solution at 180°C for 6-h under hydrothermal conditions (Figure 15B) [89]. The overall particle size and shell thickness were controlled by varying the concentration of TiF_4, by which absorption was tuned in the visible region of the spectrum. Instead of commonly used metal oxide shells, an Ag shell on an Au core was also found to effectively yield a considerable 24% enhancement in PCE [90].

3.1.3.3 Anisotropic metal nanostructures

Plasmonic metal nanostructures with different aspect ratios or shapes can have multiple plasmon resonance peaks due to multipolar resonance in different directions to generate multiple LSPR absorption. For example, metal nanorods (NRs) exhibit two spectrally separated LSPR bands due to coherent oscillations of conduction band electrons along transverse and longitudinal axes, and these LSPR bands, in particular the longitudinal mode, can be tuned by varying the aspect ratio [91, 92]. Figure 16 shows absorption spectra of the Au NR at different aspect ratios [93]. With increasing aspect ratios, the transverse resonance peak remained more or less at wavelengths between 510 and 550 nm, whereas the longitudinal resonance peak largely shifted towards longer wavelengths. In addition, anisotropic metal nanostructures with sharp edges and corners can produce intense localized fields. Therefore, by carefully tuning the aspect ratio and shape of anisotropic metal nanostructures, far-field scattering and near-field antenna effects can be simultaneously employed in DSCs for enhancing broadband light harvesting.

By incorporating Au NRs capped with AgS_2 into the photoanode of DSCs, Chang et al. observed an improvement in photocurrent by 37.6% in the 600–720 spectral region due to the longitudinal plasmon resonance (Figure 17) [94]. The AgS_2 shell was grown on Au NRs

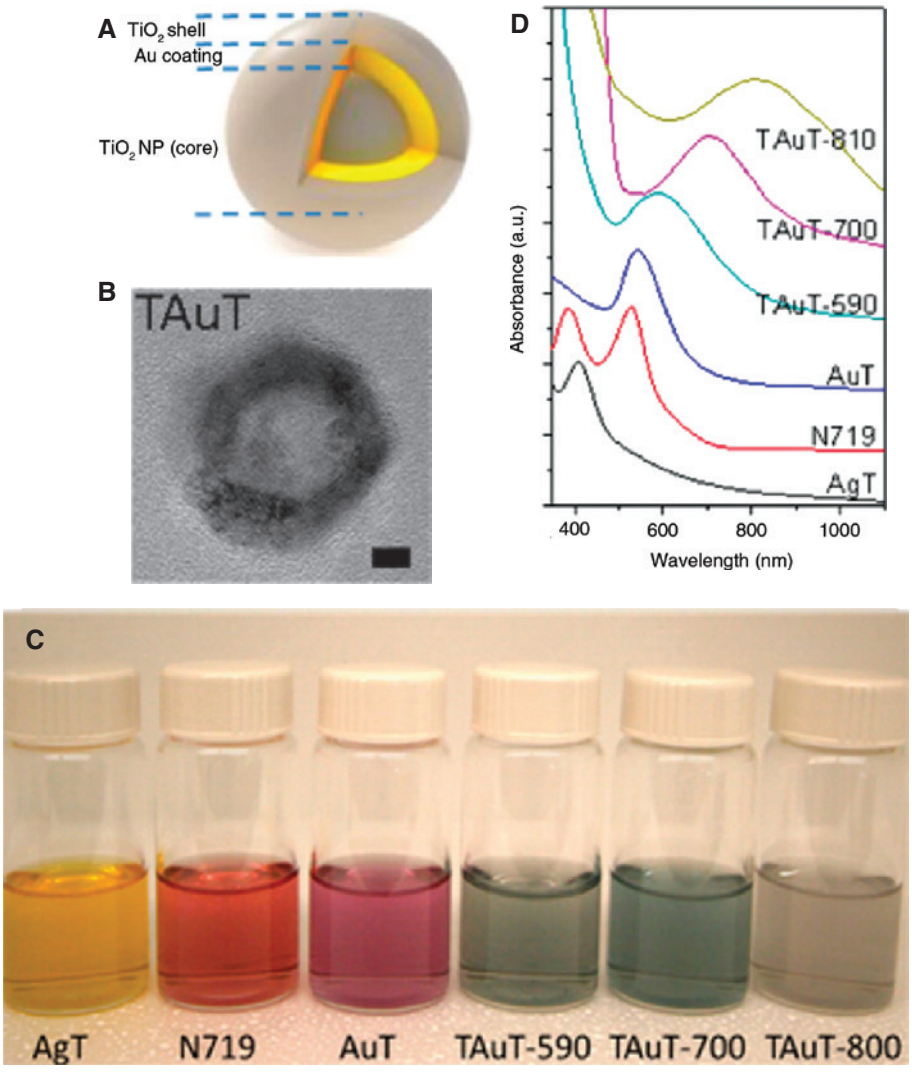

Figure 13: (A) Illustration and (B) TEM image of TiO_2@Au NP@TiO_2 nanostructure, (C) photograph and (D) absorption spectra of Ag@TiO_2, N719 dye, Au@TiO_2, TiO_2@Au NP@TiO_2-590 (λ_{LSPR}=590 nm), TiO_2@Au NP@TiO_2-700, and TiO_2@Au NP@TiO_2-810 in ethanol solutions. Reprinted with permission from [83]. Copyright 2013 American Chemical Society.

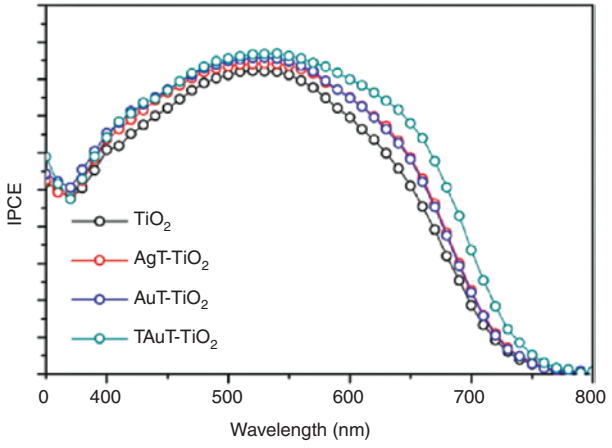

Figure 14: IPCE spectra of DSSCs with AgT, AuT, and TAuT NPs incorporated photoanodes of optimized thickness for maximum PCE. Reprinted with permission from [83]. Copyright 2013 American Chemical Society.

through reduction of Ag^+ on the surface and subsequent reaction of Na_2S with the Ag shell. The AuNR@AgS_2 displayed a longitudinal absorption peak at 685 nm, providing efficient absorption of NIR photons that dye could not usually absorb efficiently, but in the case of AgNP@AgS_2, absorption enhancement was limited to the visible regime (Figure 17B). In another study, inclusion of 2.0 wt% of AuNR@SiO_2 in the photoanode enhanced the photocurrent by 20% (Figure 17C) [95].

Highly irregular popcorn-shaped Au-Ag alloy NPs, which were synthesized by co-reduction method, could also enhance broadband light absorption as they could produce different LSP modes over a wide wavelength range [96, 97]. The PCE of DSCs was improved by 16% from 5.26% to 6.09% by incorporating 2.38 wt% of these unusually shaped metal NPs [96]. The IPCE enhancement

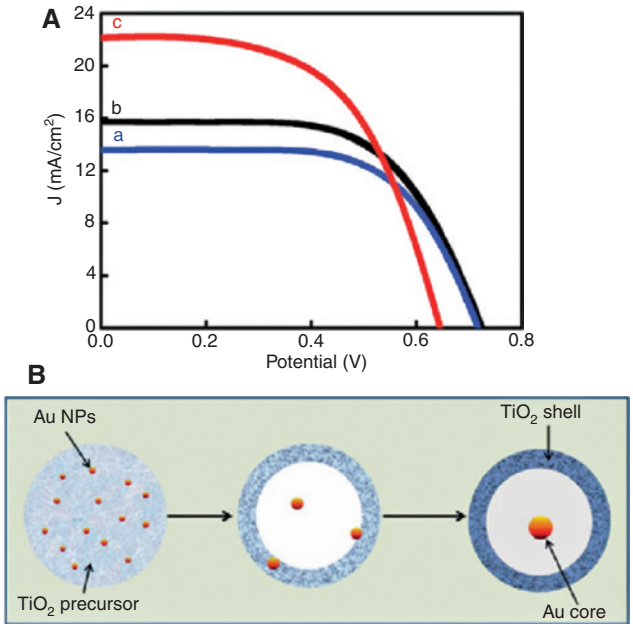

Figure 15: (A) *J–V* curves obtained by (a) P25, (b) TiO_2 hollow submicrospheres with thin shell and (c) Au@TiO_2 hollow submicrospheres with thin shell. (B) Illustrations of formation process of Au@TiO_2 hollow submicrospheres. Reproduced from [88] with permission of The Royal Society of Chemistry.

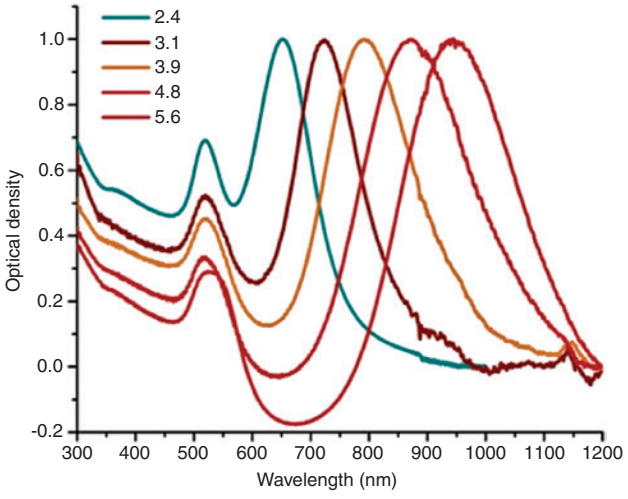

Figure 16: Surface plasmon absorption spectra of gold nanorods of different aspect ratios, showing the sensitivity of the strong longitudinal band to the aspect ratios of the nanorods. Reprinted with permission from [93]. Copyright 2006 American Chemical Society.

ratio graph clearly shows photocurrent enhancement in the 550–800-nm region of the spectrum, corresponding to the LSPR of the popcorn-shaped metal NPs (Figure 18).

Au@SiO_2 nanocubes were found advantageous over spherical NPs in DSCs, as they had two times higher

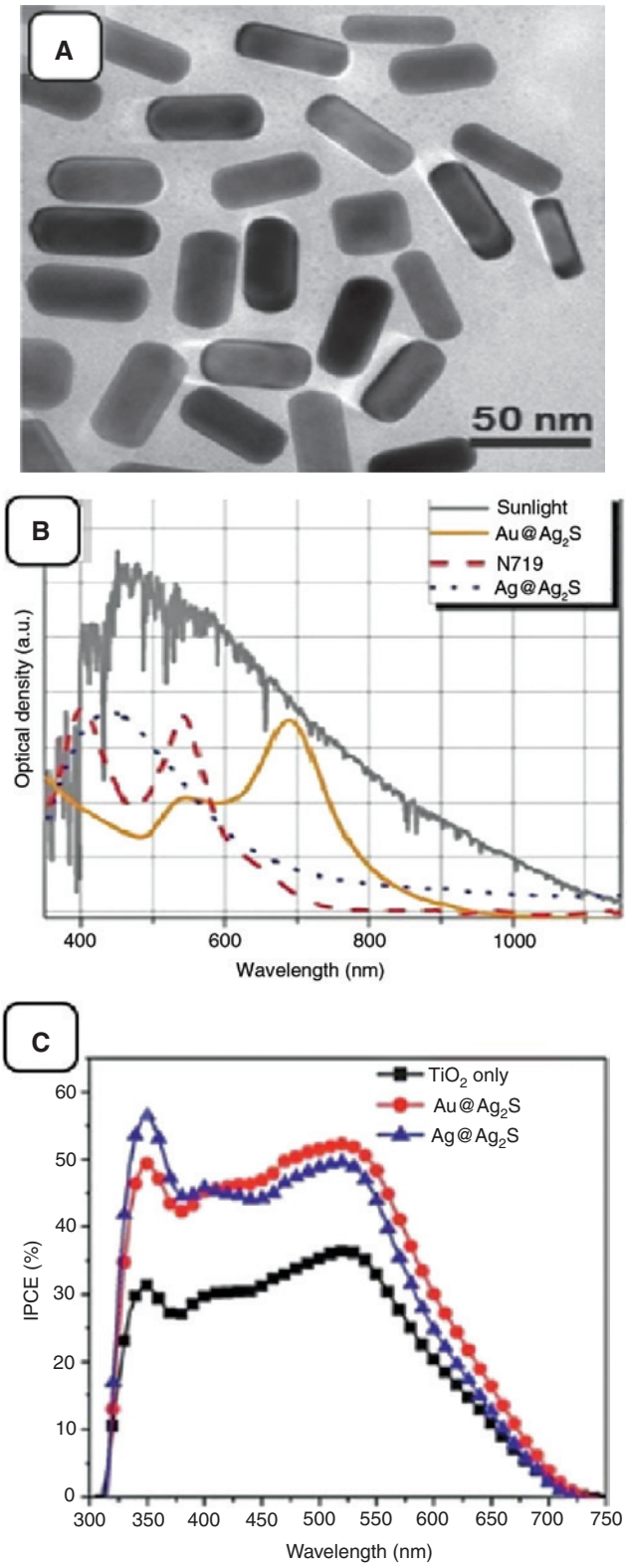

Figure 17: (A) TEM image of as-synthesized AuNR@Ag_2S, (B) Solar irradiance spectrum, absorption of AuNR@Ag_2S (2 nm in shell thickness), N719 dye solution in acetonitrile and t-butanol and Ag_2S-encapsulated Ag nanoparticles, AgNP@Ag_2S and (C) IPCE (%) of DSCs with Au@Ag_2S and Ag@Ag_2S NPs. Reproduced from [94] with permission of The Royal Society of Chemistry.

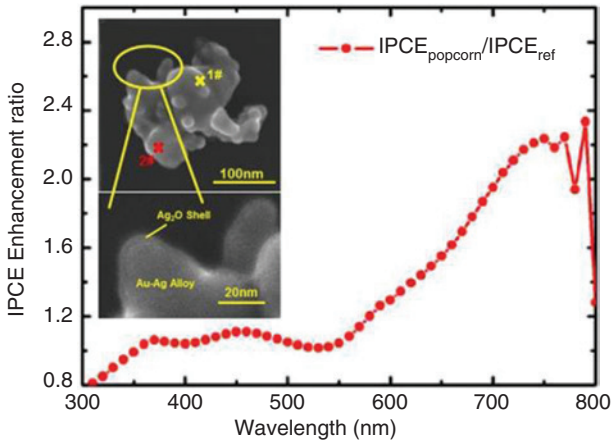

Figure 18: The IPCE enhancement ratio of the plasmonic DSCs. IPCE enhancement ratio=IPCE$_{popcorn(\lambda)}$/IPCE$_{TiO_2\text{-}only(\lambda)}$, where IPCE$_{popcorn(\lambda)}$ and IPCE$_{TiO_2\text{-}only(\lambda)}$ are the IPCEs of the popcorn NP-enhanced DSCs and TiO_2-only DSCs at wavelength λ, respectively. Scanning electron microscopy (SEM) images of popcorn NPs are shown in inset. Reprinted by permission from Macmillan Publishers Ltd. Scientific Reports [96], copyright 2013.

extinction and absorption efficiency, two times larger surface area, and higher electromagnetic field localization at edges and corners [49, 30, 98, 99]. The edge length of Au nanocubes can be adjusted by hexadecyltrimethylammonium bromide (CTAB) ligands [100]. FDTD simulations have shown that the light extinction by Au@SiO_2 nanocubes is very high in the 700–900-nm spectral region due to their very strong light scattering and absorption in this regime. When 1.8 wt% of Au@SiO_2 nanocubes were incorporated into photoanodes, the PCE was improved from 5.8% to 7.8% [30]. This impressive efficiency improvement was mainly attributed to the intense field confinement at the corners and edges of nanocubes and the far-field scattering by nanocubes.

Application of metal@SiO_2 triangular nanoprisms was also explored in DSCs [101, 102]. Incorporation of 0.05 wt% Ag@SiO_2 triangular nanoprisms into photoanodes improved PCE by 32% due to the improvement in light harvesting in the 550–750 nm spectral region, while only a 15% enhancement was observed when Au@SiO_2 triangular nanoprisms were used. Even though, PCE enhancement was better for photoanode with Ag@SiO_2 due to excellent light harvesting at the NIR spectral region, thermal and chemical stability was found to be modest compared with Au@SiO_2.

Very recently, it was found that incorporation of Au nanostars into N719 DSCs improved their PCE by ~20% from 7.1% to 8.4% (Figure 19A) [103]. Meanwhile, a 30% PCE improvement (from 3.9% to 5.0%) was obtained for

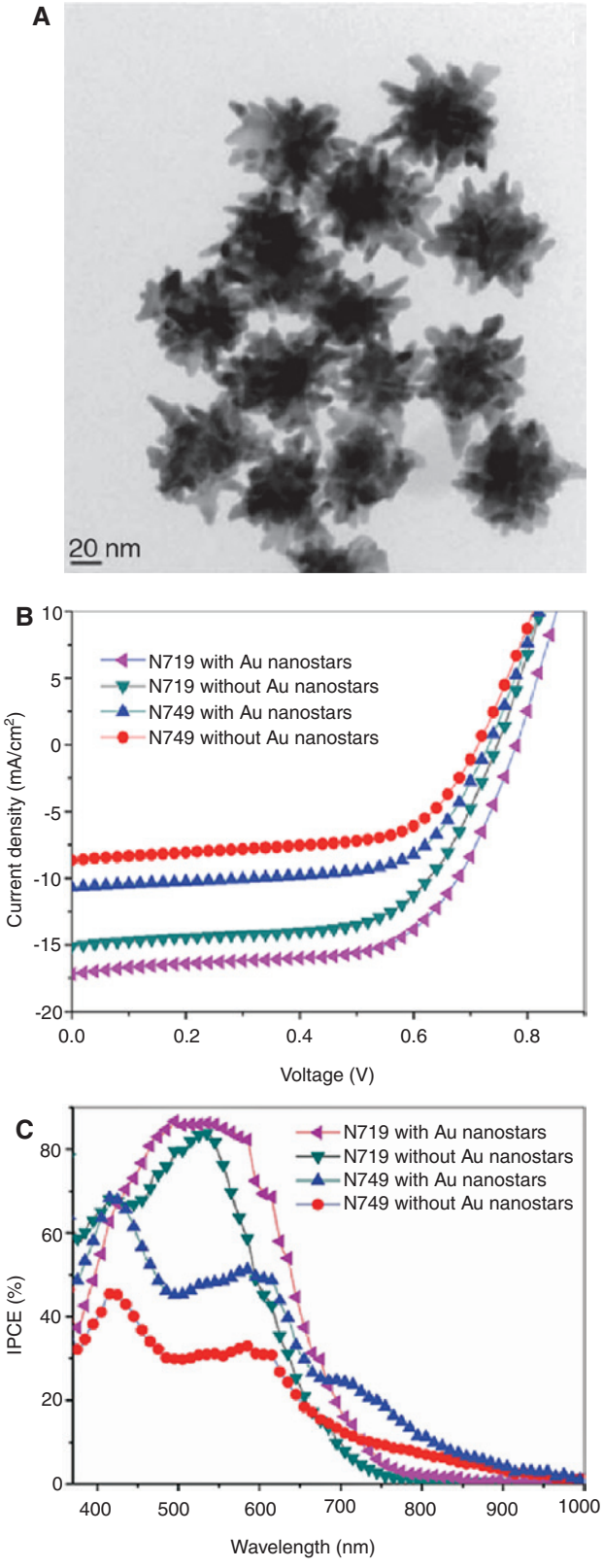

Figure 19: (A) Transmission electron microscopy (TEM) image of Au nanostars, (B) *J–V* characteristics of N719 and N749 DSSCs with and without Au nanostars, (C) IPCE action spectra for N719 and N749 DSSC devices with and without Au nanostars. Reproduced from [103] with permission of The Royal Society of Chemistry.

DSCs using N749 dye (Figure 19B). The Au nanostars exhibited broad and strong light absorption from visible to NIR with a peak at ~785 nm and thereby improved the photon-to-current conversion of the solar cells over a broad spectral range (Figure 19C).

3.2 Quantum dot solar cells

QDs have attracted considerable interest due to their excellent properties, such as high extinction coefficient, bandgap tunability, and high potential for efficient multiple exciton generation (MEG) [104–106]. The bandgap tunability and MEG of QDs are particularly useful properties for solar cell application. Although the concept of MEG has long been theoretically demonstrated in QDs for achieving dramatic enhancement in photocurrent, experimentally, it was only demonstrated recently with certain photocurrent increase in QDs based solar cells [107]. Meanwhile, efforts have been dedicated to enhance photocurrent by embedding plasmonic metal NPs in QDs based solar cells. As in the case of plasmon-enhanced DSCs, metal NPs were incorporated into QDs solar cells to enhance their photocurrent mainly through the near-field antenna effect and far-field scattering effect [17, 108, 109]. In this section, our discussion will be confined to solution processed QDs solar cells, including planar and BHJ configurations. The schematic description of both configurations is depicted in Figure 20. The reports on plasmon-enhanced QDs based solar cells are very limited, and true potential of plasmonic metal nanostructures in QDs based solar cells remain largely unexplored.

Kawawaki et al. explored application of Ag NPs in PbS QD/ZnO nanowire BHJ solar cells [110]. FDTD simulations revealed that Ag and Au nanocubes have strong light scattering in the wavelength range of 700–1200 nm compared to their spherical counterparts. In addition, Ag nanocubes have weaker absorption in the wavelength range of 300–450 nm, which helps to avoid blocking of light absorption by PbS QDs. The PCE was improved by 1.36 times when Ag nanocubes were incorporated into PbS QD/ZnO nanowire BHJ solar cells. The position of metal NPs in QD BHJ solar cells is very important for soliciting plasmonic effects. For the optimization, the authors incorporated metal NPs by spin coating at different locations in the device. It was found that photocurrent was reduced when metal NPs were incorporated close to transparent conductive oxide (TCO) substrate or Au counter electrodes. When the metal NPs were too close to the illuminated side (i.e. TCO), absorption of light by QDs was reduced significantly because of the parasitic absorption by metal NPs in the visible spectra. In the second case, metal NPs were far away from the electron acceptor, i.e. ZnO, so the photocurrent was limited by hole-electron recombination or unsuccessful utilization of the near-field effect. Interestingly, when metal NPs were close to ZnO nanowire, both V_{oc} and FF values of these devices were significantly lower than those without metal NPs because the metal NPs in contact with the electron acceptor acted as a leakage path (back electron transfer), which lowered the Fermi level of the electron acceptor and the parallel resistance of solar cells as well. Three-dimensional FDTD simulations show that the best location for the inclusion of metal NPs is 260 nm away from the illuminated side of colloidal QD (CQD) film [111]. In planar configuration, the maximum photocurrent enhancement obtained when metal NPs were incorporated at the distance of 220–260 nm from the illuminated side of QD film [110]. Figure 21A shows the absorption spectra of 400-nm-thick PbS CQD film with metal NPs at different locations [111]. As mentioned above, metal NPs were embedded in CQD solar cells by spin coating metal NP containing solution. For both configurations, the

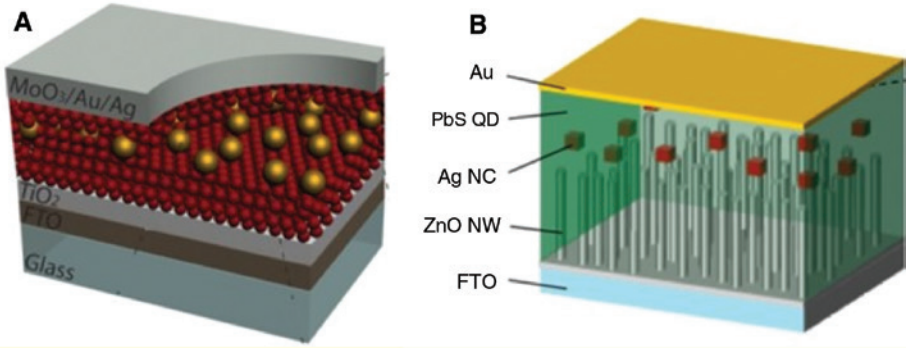

Figure 20: Schematic of typical device architectures of (A) planar colloidal quantum dot solar cells. Reprinted (adapted) with permission from [110]. Copyright 2015 American Chemical Society. (B) quantum dot bulk-heterojunction solar cells. Reprinted (adapted) with permission from [111]. Copyright 2013 American Chemical Society.

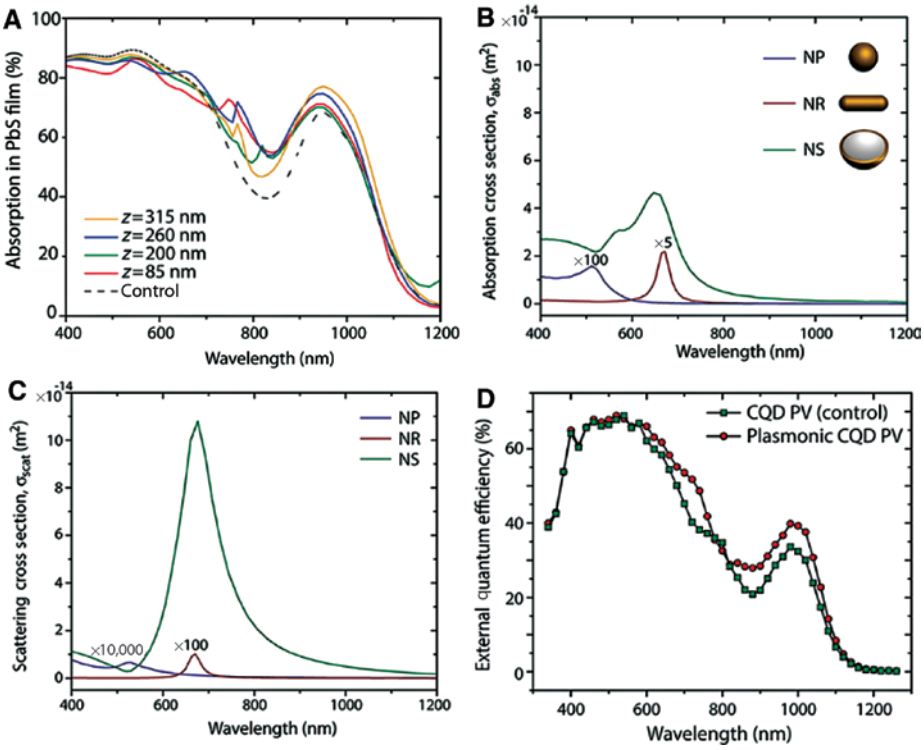

Figure 21: 3D FDTD simulation of plasmonic-excitonic films. (A) Absorption spectra (including back-reflector) in a 400-nm-thick PbS quantum dot film with nanoshells embedded at different values of *z*, the distance from the PbS bottom-illuminated interface to the center of the nanoshells. The nanoshells are periodically spaced by an average of 300 nm, (B) absorption and (C) scattering cross-section spectra as a function of shape, (D) external quantum efficiency spectra of control and plasmonic CQD solar cells. A peak 35% enhancement centered at a wavelength of 880 nm was observed in the plasmonic device. Reprinted with permission from [111]. Copyright 2013 American Chemical Society.

optimum concentration of the metal NPs in spin coating solutions was found to be 20–30 mg mL^{-1} [110, 111].

Paz-Soldan et al. theoretically evaluated the impact of differently shaped Au NPs in planar CQD solar cells using FDTD [111]. They found that spherical dielectric metal oxide core@metal shell NPs (named as nanoshells) were more appropriate for the CQD solar cell application compared with spherical NPs and NRs because the scattering-to-absorption ratio of the former was significantly higher than the latter nanostructures (Figure 21B and C). Moreover, theoretical calculations have shown that 150-nm-sized nanoshell has high scattering to absorption ratio compared to largely sized NRs (66 nm in diameter and 512 nm in length). In thin film solar cells like CQD devices, lesser sized metal NPs with higher scattering-to-absorption ratio are preferred considering the difficulty in incorporating bigger metal NPs into thin films. Inclusion of nanoshells in CQD solar cells improved the efficiency of solar cells by 11% (from 6.2% to 6.9%). Enhancement in the overall PCE is attributed to improved photocurrent in the NIR spectral region, especially a 35% enhancement observed at 880 nm (Figure 21D).

3.3 Perovskite solar cells (PSCs)

Solar cells based on perovskite absorbers promise highly efficient solar energy conversion at low cost [112–114]. Hybrid inorganic-organic perovskites are the class of materials that adopt crystal structure of ABX_3, where generally 'A' denotes a large organic or inorganic cation, 'B' a metal cation, and 'X' is a halide anion. The inorganic-organic lead halide perovskite ($CH_3NH_3PbI_3$) has achieved a remarkable performance with a certified efficiency of 22.1% in the short span of time [115]. Three different types of solar cell configurations (Figure 22) have been explored in PSCs, (1) p-i-n heterojunction: the perovskite absorber deposited on a compact layer of semiconductor oxide; (2) perovskite sensitized solar cells: a mesoporous semiconductor oxide film sensitized with the perovskite absorber; and (3) meso-superstructured solar cells: the perovskite absorber deposited on an inert scaffold and charge carriers transported through the perovskite absorber itself [116]. To date, there are only a few reports on plasmon-enhanced PSCs [117–119].

Plasmon-enhanced PSCs have only been realized in perovskite sensitized and meso-superstructured solar

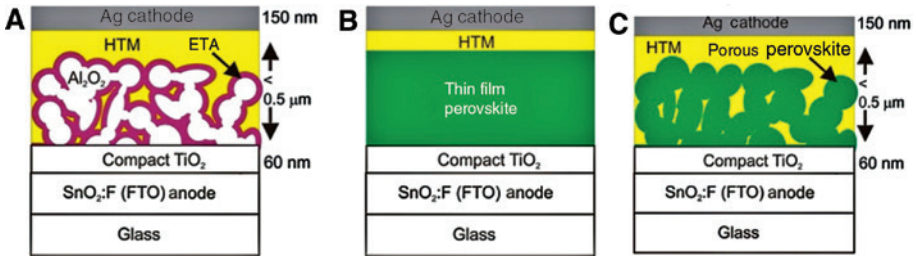

Figure 22: Schematic depiction of (A) meso-superstructured solar cell, (B) thin-film p–i–n perovskite solar cell, and (C) perovskite sensitized solar cell. Reprinted with permission from [116]. Copyright 2013 American Chemical Society.

cell configurations [118, 120]. To invoke plasmonic effects in PSCs, metal NPs were incorporated into inert or semiconducting oxide scaffolds that support the perovskite absorber. Figure 23A shows cross-sectional scanning electron microscope image of a perovskite meso-superstructured solar cell. In general, the optimum concentration of spherical metal NPs was found to be 0.8–0.9 wt% [117, 120]. Interestingly, Zhang et al. found that photocurrent enhancement in their developed plasmon-enhanced PSCs arose from the reduction of exciton binding energy with the integration of core@shell Au@SiO_2 NPs into an alumina scaffold [117]. Instead, they could not observe any near-field effects or absorption enhancement. Recently, the same research group put forward a new mechanism called 'plasmonic-induced photon recycling' to explain photocurrent enhancement [120]. This mechanism can be explained as follows: highly polarizable metal NPs can act as optical antennas by providing extended optical path length to the reemitted photons from the perovskite absorbers due to the exciton decay, so the reemitted light can be reabsorbed by the perovskite absorbers (i.e. photons are recycled) with the help of metal NPs [121, 122]. According to the authors, it is the plasmonic-induced photon recycling by Ag@TiO_2 that improved the average PCE from 11.4%±1.3% to 13.7±1.2% (Figure 23B) [120].

In contrary, Lu et al. reported that including Au-Ag alloy popcorn-shaped NPs enhanced the photocurrent through improved light absorption [118]. As we discussed in the previous Section of 2.2.4, popcorn-shaped metal NPs exhibited various LSP modes, leading to enhanced broadband light absorption [96]. Carretero-Palacios et al. analyzed absorption enhancement in perovskite films with embedded Au NPs using 3D FDTD simulations. Near-field effects were found to dominate when the metal NPs are close to the glass substrate, while scattering effects predominate when NPs are located near the hole transporting medium (spiro-OMeTAD) [123]. The maximum extinction of light occurs when the NPs are located at the center of the perovskite film with the contributions from both plasmonic near-field and scattering effects. Figure 24A depicts theoretical

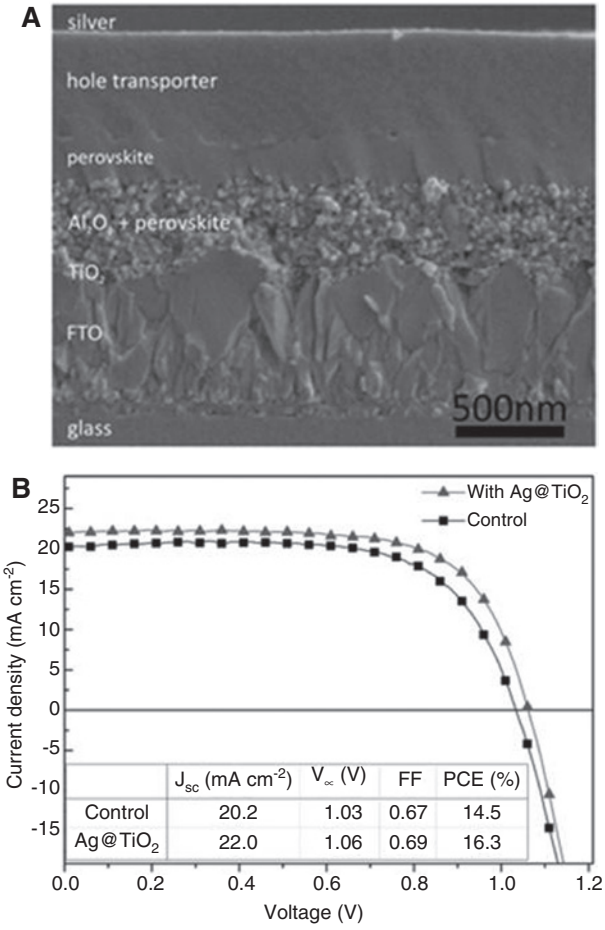

Figure 23: (A) SEM cross-section of a meso-superstructured solar cell (MSSC), (B) current density-voltage characteristics for the best control device and optimized Ag@TiO_2 device. The solar cells were measured via scanning from 1.4 V to short circuit at a scan rate of 0.15 V s^{-1}. Reprinted with permission from [120]. Copyright 2015 WILEY-VCH Verlag GmbH & Co. KGaA, Weinheim.

perovskite solar absorption enhancement as function of the location of an Au NP inside the perovskite slab. Absorption spectra calculated at several z positions are plotted in Figure 24B. Although a comprehensive understanding on all relevant mechanisms of plasmon-enhanced PSCs is yet to be evolved, a faster charge transport has been observed

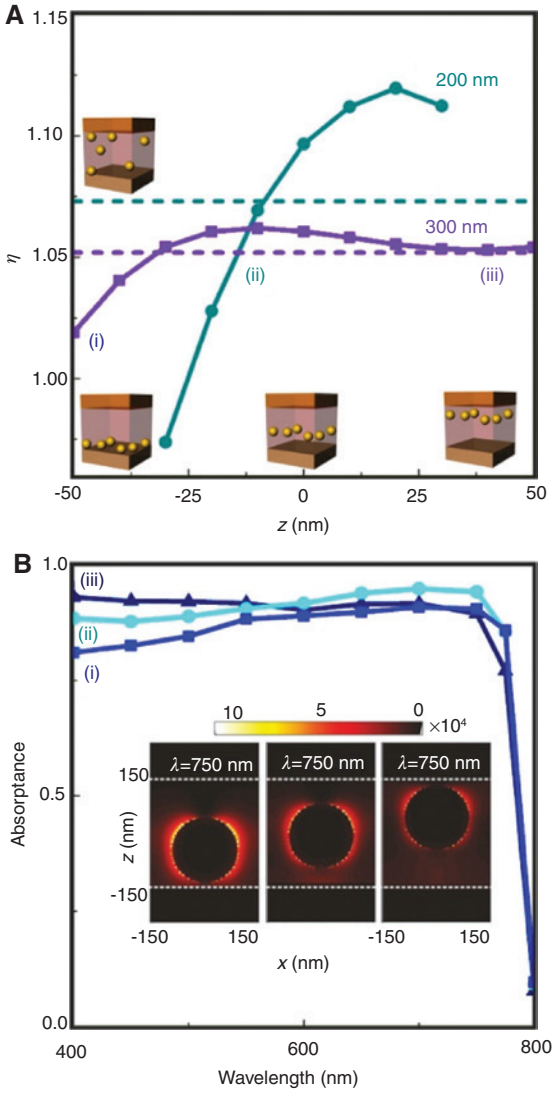

Figure 24: (A) Perovskite solar absorption enhancement, η, as a function of the z position of the AuNP inside the perovskite slab. Circles account for a 200×200×200-nm^3 system with a sphere of r=60 nm and squares for a 300×300×300 nm^3 with a sphere of r=90nm. Dashed lines correspond to the average value for all z positions in each case. (B) For the 300×300×300-nm^3 case, absorption spectra at several z positions, (i) z=−50 nm, (ii) z=−10 nm, and (iii) z=+50 nm. Colors correspond to the positions indicated in panel (A). The inset displays corresponding absorption profile at λ=750 nm.

in most of the reports on plasmon-enhanced PSCs, to the best of our knowledge [117, 118, 120].

The QD solar cells and PSCs share a lot of common aspects, such as device architecture and a thin photoactive layer. On a closer look, it is evident that first principles for inclusion of plasmonic nanostructures (like position of plasmonic nanostructures, requirement of high scattering-to-absorption ratio, etc.) in these devices are the same in most of the cases, although the exact mechanism of PCE enhancement in plasmonic PSCs is yet to be further evolved.

4 Conclusions and future outlook

Generally, third-generation solar cells lag behind silicon solar cells in efficiency mainly due to inefficient light absorption, so light management in third-generation solar cells is essential to achieve a high overall PCE. In plasmon-enhanced solar cells, near-field effects and far-field scattering by plasmonic metal NPs can be utilized to increase the extinction cross-section of the solar cells and hence the PCE. Inclusion of metal nanostructures enables physically very thin PV absorbers of the third-generation solar cells to be optically thick.

Even though there are some extensive researches done on the plasmon-enhanced organic solar cells and DSCs, plasmonic effects in perovskite and QDs based solar cells remain largely unexplored. In addition, the efficiency of most of these solar cells needs to be further improved. In order to achieve the highest gain in PCE from plasmonic nanostructures, it is important to intelligently design and realize in a controlled fashion plasmonic metal nanostructures with desired size, shape, and morphology (such as core@shell). Similarly important, the way to integrate plasmonic nanostructures into these solar cells is another major factor to consider. Theoretical calculations can provide guidance to the rational and more efficient development on all these aspects from materials design to device structure construction and are thus highly required. Moreover, better understanding of involved enhancement mechanisms is needed. For instance, the exact mechanism regarding the photocurrent enhancement in the perovskite solar cells with plasmonic metal NPs is still unclear at present. A comprehensive scientific research by correlating experimental results with simulations is essential to reveal the fundamental understanding of plasmonic effects in perovskite absorbers as well as in other solar cells. In this review, we have tried to give a clear, up-to-date account of several types of plasmonic-enhanced third generation solar cells. The integration of two hot topics (plasmonics and solar energy conversion) in materials science is expected to provide a new outlook for finding an amicable solution for the energy crisis.

References

[1] Leonhardt U. Optical metamaterials: invisibility cup. Nat Photonics 2007;1:207–8.
[2] Thompson D. Michael Faraday's recognition of ruby gold: the birth of modern nanotechnology. Gold Bull 2007;40:267–9.
[3] Yamamoto M. Surface plasmon resonance (SPR) theory: tutorial. Rev Polarogr 2008;48:1–32.

[4] Homola J, Piliarik M. Surface plasmon resonance (SPR) sensors. In: Jiří H, ed. Surface plasmon resonance based sensors, 1st ed. Berlin, Heidelberg, Germany; Springer-Verlag, 2006:45–67.
[5] Anker JN, Hall WP, Lyandres O, Shah NC, Zhao J, Van Duyne RP. Biosensing with plasmonic nanosensors. Nat Mater 2008;7:442–53.
[6] Kabashin AV, Evans P, Pastkovsky S, Hendren W, Wurtz GA, Atkinson R, Pollard R, Podolskiy VA, Zayats AV. Plasmonic nanorod metamaterials for biosensing. Nat Mater 2009;8: 867–71.
[7] Liu Z, Steele JM, Srituravanich W, Pikus Y, Sun C, Zhang X. Focusing surface plasmons with a plasmonic lens. Nano Lett 2005;5:1726–9.
[8] Xu G, Liu J, Wang Q, Hui R, Chen Z, Maroni VA, Wu J. Plasmonic graphene transparent conductors. Adv Mater 2012;24:OP71–6.
[9] Reddy KG, Deepak TG, Anjusree GS, Thomas S, Vadukumpully S, Subramanian KR, Nair SV, Nair AS. On global energy scenario, dye-sensitized solar cells and the promise of nanotechnology. Phys Chem Chem Phys 2014;16:6838–58.
[10] Turner JA. A realizable renewable energy future. Science 1999;285:687–9.
[11] Ferry VE, Verschuuren MA, Li HBT, Verhagen E, Walters RJ, Schropp RE, Atwater HA, Polman A. Light trapping in ultrathin plasmonic solar cells. Opt Express 2010;18:A237–45.
[12] Hagfeldt A, Boschloo G, Sun L, Kloo L, Pettersson H. Dye-sensitized solar cells. Chem Rev 2010;110:6595–663.
[13] Pattantyus-Abraham AG, Kramer IJ, Barkhouse AR, Wang X, Konstantatos G, Debnath R, Levina L, Raabe I, Nazeeruddin MK, Grätzel M, Sargent EH. Depleted-heterojunction colloidal quantum dot solar cells. ACS Nano 2010;4:3374–80.
[14] Tachibana Y, Vayssieres L, Durrant JR. Artificial photosynthesis for solar water-splitting. Nat Photonics 2012;6:511–18.
[15] Holladay JD, Hu J, King DL, Wang Y. An overview of hydrogen production technologies. Catal Today 2009;139:244–60.
[16] Schlapbach L, Züttel A. Hydrogen-storage materials for mobile applications. Nature 2001;414:353–58.
[17] Catchpole KR, Polman A. Plasmonic solar cells. Opt Express 2008;16:21793–800.
[18] Atwater HA, Polman A. Plasmonics for improved photovoltaic devices. Nat Mater 2010;9:205–13.
[19] Kim S-S, Na S-I, Jo J, Kim D-Y, Nah Y-C. Plasmon enhanced performance of organic solar cells using electrodeposited Ag nanoparticles. Appl Phys Lett 2008;93:073307.
[20] Ferry VE, Sweatlock LA, Pacifici D, Atwater HA. Plasmonic nanostructure design for efficient light coupling into solar cells. Nano Lett 2008;8:4391–7.
[21] Zhang X, Chen YL, Liu R-S, Tsai DP. Plasmonic photocatalysis. Rep Prog Phys 2013;6:046401.
[22] Linic S, Christopher P, Ingram DB. Plasmonic-metal nanostructures for efficient conversion of solar to chemical energy. Nat Mater 2011;10:911–21.
[23] Maier SA. Plasmonics: fundamentals and applications. Springer US, Springer-Verlag US, 2007.
[24] Kelly KL, Coronado E, Zhao L, Schatz GC. The optical properties of metal nanoparticles: the influence of size, shape, and dielectric environment. J Phys Chem B 2003;107:668–77.
[25] Lee J-Y, Peumans P. The origin of enhanced optical absorption in solar cells with metal nanoparticles embedded in the active layer. Opt Express 2010;18:10078–87.
[26] Jackson JD. Classical electrodynamics. New Yark, USA: Jhon Wiley & sons Inc., 1999.
[27] Griffiths DJ. Introduction to electrodynamics. Harlow, UK: Pearson Education Limited, 2014.
[28] Li M, Cushing SK, Zhang J, Lankford J, Aguilar ZP, Ma D, Wu N. Shape-dependent surface-enhanced Raman scattering in gold–Raman-probe–silica sandwiched nanoparticles for biocompatible applications. Nanotechnology 2012;23:115501.
[29] Wang H, Brandl DW, Nordlander P, Halas NJ. Plasmonic nanostructures: artificial molecules. Acc Chem Res 2007;40:53–62.
[30] Zarick HF, Hurd O, Webb JA, Hungerford C, Erwin WR, Bardhan R. Enhanced efficiency in dye-sensitized solar cells with shape-controlled plasmonic nanostructures. ACS Photonics 2014;1:806–11.
[31] El-Sayed MA. Some interesting properties of metals confined in time and nanometer space of different shapes. Acc Chem Res 2001;34:257–64.
[32] Kawawaki T, Takahashi Y, Tatsuma T. Enhancement of dye-sensitized photocurrents by gold nanoparticles: effects of plasmon coupling. J Phys Chem C 2013;117:5901–07.
[33] Stuart HR, Hall DG. Absorption enhancement in silicon-on-insulator waveguides using metal island films. Appl Phys Lett 1996;69:2327–29.
[34] Beck FJ, Polman A, Catchpole KR. Tunable light trapping for solar cells using localized surface plasmons. J Appl Phys 2009;105:1–7.
[35] Bohren CF, Huffman DR. Absorption and scattering of light by small particles. Germany: WILEY-VCH Verlag GmbH & Co., KGaA, 1998.
[36] Jain PK, Lee KS, El-Sayed IH, El-Sayed MA. Calculated absorption and scattering properties of gold nanoparticles of different size, shape, and composition: applications in biological imaging and biomedicine. J Phy Chem B 2006;110:7238–48.
[37] Shah AV, Schade H, Vanecek M, Meier J, Vallat-Sauvain E, Wyrsch N, Kroll U, Droz C, Bailat J. Thin-film silicon solar cell technology. Prog Photovoltaics Res Appl 2004;12:113–42.
[38] Szlufcik J, Sivoththaman S, Nijs JF, Mertens RP, Overstraeten R Van. Low-cost industrial technologies for crystalline silicon solar cells. Proceedings of the IEEE 2012;85:711–30.
[39] Green MA. Third generation photovoltaics: Solar cells for 2020 and beyond. Phys E Low-Dimensional Syst Nanostructures 2002;14:65–70.
[40] Palm J, Probst V, Karg FH. Second generation CIS solar modules. Sol Energy 2004;77:757–65.
[41] Chhajed S, Schubert MF, Kim JK, Schubert EF. Nanostructured multilayer graded-index antireflection coating for Si solar cells with broadband and omnidirectional characteristics. Appl Phys Lett 2008;93:122–24.
[42] Zhao J, Wang A, Green MA, Ferrazza F. 19.8% efficient "honeycomb" textured multicrystalline and 24.4% monocrystalline silicon solar cells. Appl Phys Lett 1998;1991:1991–3.
[43] Grätzel M. Dye-sensitized solar cells. J Photochem Photobiol C Photochem Rev 2003;4:145–53.
[44] Yella A, Lee H-W, Tsao HN, Yi C, Chandiran AK, Nazeeruddin MK, Diau EW, Yeh CY, Zakeeruddin SM, Grätzel M. Porphyrin-sensitized solar cells with cobalt (II/III)-based redox electrolyte exceed 12 percent efficiency. Science 2011;334:629–34.
[45] Li Y, Wang H, Feng QY, Zhou G, Wang ZS. Gold nanoparticles inlaid TiO2 photoanodes: a superior candidate for

high-efficiency dye-sensitized solar cells. Energy Environ Sci 2013;6:2156–65.
[46] Hou W, Pavaskar P, Liu Z, Theiss J, Aykol M, Cronin SB. Plasmon resonant enhancement of dye sensitized solar cells. Energy Environ Sci 2011;4:4650-5.
[47] Lin S-J, Lee K-C, Wu J-L, Wu J-Y. Enhanced performance of dye-sensitized solar cells via plasmonic sandwiched structure. Appl Phys Lett 2011;99:043306.
[48] Amiri O, Salavati-Niasari M, Farangi M, Mazaheri M, Bagheri S. Stable plasmonic-improved dye sensitized solar cells by silver nanoparticles between titanium dioxide layers. Electrochem Acta 2015;152:101–7.
[49] Jang YH, Jang YJ, Kochuveedu ST, Byun M, Lin Z, Kim DH. Plasmonic dye-sensitized solar cells incorporated with Au-TiO_2 nanostructures with tailored configurations. Nanoscale 2014;6:1823–32.
[50] Sebo B, Huang N, Liu Y, Tai Q, Liang L, Hu H, Xu S, Zhao X-Z. Dye-sensitized solar cells enhanced by optical absorption, mediated by TiO_2 nanofibers and plasmonics Ag nanoparticles. Electrochem Acta 2013;112:458–64.
[51] Link S, El-Sayed MA. Spectral properties and relaxation dynamics of surface plasmon electronic oscillations in gold and silver nanodots and nanorods. J Phys Chem B 1999;103:8410–26.
[52] Link S, El-Sayed MA. Size and temperature dependence of the plasmon absorption of colloidal gold nanoparticles. J Phys Chem B 1999;103:4212–7.
[53] Jeong NC, Prasittichai C, Hupp JT. Photocurrent enhancement by surface plasmon resonance of silver nanoparticles in highly porous dye-sensitized solar cells. Langmuir 2011;27:14609–14.
[54] Wang Q, Butburee T, Wu X, Chen HJ, Liu G, Wang LZ. Enhanced performance of dye-sensitized solar cells by doping Au nanoparticles into photoanodes: a size effect study. J Mater Chem A 2013;1:13524–31.
[55] Subramanian V, Wolf EE, Kamat PV. Catalysis with TiO_2/gold nanocomposites. Effect of metal particle size on the fermi level equilibration. J Am Chem Soc 2004;126:4943–50.
[56] Choi H, Chen WT, Kamat PV. Know thy nano neighbor. Plasmonic versus electron charging effects of metal nanoparticles in dye-sensitized solar cells. ACS Nano 2012;6:4418–27.
[57] Li Y, Pang A, Wang C, Wei M. Metal–organic frameworks: promising materials for improving the open circuit voltage of dye-sensitized solar cells. J Mater Chem 2011;21:17259–64.
[58] Muduli S, Game O, Dhas V, Vijayamohanan K, Bogle KA, Valanoor N, Ogale SB. TiO_2-Au plasmonic nanocomposite for enhanced dye-sensitized solar cell (DSSC) performance. Sol Energy 2012;86:1428–34.
[59] Dong H, Wu Z, El-Shafei A, Xia B, Xi J, Ning S, Jiao B, Hou X. Ag-encapsulated Au plasmonic nanorods for enhanced dye-sensitized solar cell performance. J Mater Chem A 2015;3:4659–68.
[60] Standridge SD, Schatz GC, Hupp JT. Distance dependence of plamson-enhanced photocurrent in dye-sensitized solar cells. J Am Chem Soc 2009;131:8407–9.
[61] Kreibig U and Vollmer M. Optical Properties of Metal Clusters. Berlin, Heidelberg, Germany: Springer-Verlag, 1995.
[62] Zhao G, Kozuka H, Yoko T. Effects of the incorporation of silver and gold nanoparticles on the photoanodic properties of rose bengal sensitized TiO_2 film electrodes prepared by sol-gel method. Sol Energy Mater Sol Cells 1997;46:219–31.
[63] Ihara M, Tanaka K, Sakaki K, Honma I, Yamada K. Enhancement of the absorption coefficient of cis-(NCS)(2) bis(2,2′-bipyridyl-4,4′-dicarboxylate)ruthenium(II) dye in dye-sensitized solar cells by a silver island film. J Phys Chem B 1997;101:5153–7.
[64] Xiong Y, Wang Y, Wang H, Wang R, Cui Z. Novel one-step synthesis to cross-linked polymeric nanoparticles as highly active and selective catalysts for cycloaddition of CO_2 to epoxides. J Appl Polym Sci 2012;123:1486–93.
[65] Peh CKN, Ke L, Ho GW. Modification of ZnO nanorods through Au nanoparticles surface coating for dye-sensitized solar cells applications. Mater Lett 2010;64:1372–5.
[66] Sheehan SW, Noh H, Brudvig GW, Cao H, Schmuttenmaer CA. Plasmonic enhancement of dye-sensitized solar cells using core–shell–shell nanostructures. J Phys Chem C 2013;117: 927–34.
[67] Jung H, Koo B, Kim J, Kim T, Son HJ, Kim B, Kim JY, Lee DK, Kim H, Cho J, Ko MJ. Enhanced photovoltaic properties and long-term stability in plasmonic dye-sensitized solar cells via noncorrosive redox mediator. ACS Appl Mater Interfaces 2014;6:19191–200.
[68] Nakao Y, Soneb K. Reversible dissolutioddeposition of gold in iodine-iodide-acetonitrile systems. Chem Commun 1996; 897–898.
[69] Standridge SD, Schatz GC, Hupp JT. Toward plasmonic solar cells: protection of silver nanoparticles via atomic layer deposition of TiO_2. Langmuir 2009;25:2596–600.
[70] Chen H, Blaber MG, Standridge SD, DeMarco EJ, Hupp JT, Ratner MA, Schatz GC. Computational modeling of plasmon-enhanced light absorption in a multicomponent dye sensitized solar cell. J Phys Chem C 2012;116:10215–21.
[71] Qi J, Dang X, Hammond PT, Belcher AM. Highly efficient plasmon-enhanced dye-sensitized solar cells through metal@ oxide core-shell nanostructure. ACS Nano 2011;5:7108–16.
[72] Brown MD, Suteewong T, Kumar RSS, D'Innocenzo V, Petrozza A, Lee MM, Wiesner U, Snaith HJ. Plasmonic dye-sensitized solar cells using core–shell metal–insulator nanoparticles. Nano Lett 2011;11:438–45.
[73] Liz-Marzán LM, Giersig M, Mulvaney P. Synthesis of nanosized gold-silica core-shell particles. Langmuir 1996;12:4329–35.
[74] Enustun BV, Turkevich J. Coagulation of colloidal gold. J Am Chem Soc 1963;85:3317–28.
[75] Stöber W, Fink A, Bohn E. Controlled growth of monodisperse silica spheres in the micron size range. J Colloid Interface Sci 1968;26:62–9.
[76] Vanderkooy A, Brook MA. Polyvinylpyrrolidone molecular weight controls silica shell thickness on Au nanoparticles with diglycerylsilane as precursor. ACS Appl Mater Interfaces 2012;4:3980–6.
[77] Vanderkooy A, Chen Y, Gonzaga F, Brook MA. Silica shell/gold core nanoparticles: Correlating shell thickness with the plasmonic red shift upon aggregation. ACS Appl Mater Interfaces 2011;3:3942–7.
[78] Kobayashi Y, Inose H, Nakagawa T, Gonda K, Takeda M, Ohuchi N, Kasuya A. Control of shell thickness in silica-coating of Au nanoparticles and their X-ray imaging properties. J Colloid Interface Sci 2011;358:329–33.
[79] Graf C, Vossen DLJ, Imhof A, Van Blaaderen A. A general method to coat colloidal particles with silica. Langmuir 2003;19:6693–700.
[80] Liu S, Han MY. Silica-coated metal nanoparticles. Chem An Asian J 2010;5:36–45.

[81] Joo SH, Park JY, Tsung C-K, Yamada Y, Yang P, Somorjai GA. Thermally stable Pt/mesoporous silica core–shell nanocatalysts for high-temperature reactions. Nat Mater 2009;8: 126–31.
[82] Liu W-L, Lin F-C, Yang Y-C, Huang CH, Gwo S, Huang MH, Huang JS. The influence of shell thickness of Au@TiO_2 core-shell nanoparticles on the plasmonic enhancement effect in dye-sensitized solar cells. Nanoscale 2013;5:7953–62.
[83] Dang X, Qi J, Klug MT, Chen PY, Yun DS, Fang NX, Hammond PT, Belcher AM. Tunable localized surface plasmon-enabled broadband light-harvesting enhancement for high-efficiency panchromatic dye-sensitized solar cells. Nano Lett 2013;13:637–42.
[84] Spuch-Calvar M, Pérez-Juste J, Liz-Marzán LM. Hematite spindles with optical functionalities: Growth of gold nanoshells and assembly of gold nanorods. J Colloid Interface Sci 2007;310:297–301.
[85] Daniel MC, Astruc D. Gold nanoparticles: assembly, supramolecular chemistry, quantum-size-related properties, and applications toward biology, catalysis, and nanotechnology. Chem Rev 2004;104:293–346.
[86] Cortie MB, McDonagh AM. Synthesis and optical properties of hybrid and alloy plasmonic nanoparticles. Chem Re 2011;111:3713–35.
[87] Klinkova A, Choueiri RM, Kumacheva E. Self-assembled plasmonic nanostructures. Chem Soc Rev 2014;43:3976–91.
[88] Du J, Qi J, Wang D, Tang Z. Facile synthesis of Au@TiO_2 core–shell hollow spheres for dye-sensitized solar cells with remarkably improved efficiency. Energy Environ Sci 2012;5:6914-8.
[89] Li J, Hua CZ. Size tuning, functionalization, and reactivation of Au in TiO_2 nanoreactors. Angew Chemie Int Ed 2005;44: 4342–5.
[90] Yun J, Hwang SH, Jang J. Fabrication of Au@Ag core/shell nanoparticles decorated TiO_2 hollow structure for efficient light-harvesting in dye-sensitized solar cells. ACS Appl Mater Interfaces 2015;7:2055–63.
[91] Aizpurua J, Bryant GW, Richter LJ, García De Abajo FJ, Kelley BK, Mallouk T. Optical properties of coupled metallic nanorods for field-enhanced spectroscopy. Phys Rev B -Condens Matter Mater Phys 2005;71:1–13.
[92] Link S, Mohamed MB, El-Sayed MA. Simulation of the optical absorption spectra of gold nanorods as a function of their aspect ratio and the effect of the medium dielectric constant. J Phys Chem B 1999;103:3073–7.
[93] Huang X, El-sayed IH, Qian W, El-sayed MA. Cancer cell imaging and photothermal therapy in the near-infrared region by using gold nanorods. J Am Chem Soc 2006;128:2115–20.
[94] Chang S, Li Q, Xiao X, Wong KY, Chen T. Enhancement of low energy sunlight harvesting in dye-sensitized solar cells using plasmonic gold nanorods. Energy Environ Sci 2012;5:9444–8.
[95] Bai L, Li M, Guo K, Luoshan M, Fatima H. Plasmonic enhancement of the performance of dye-sensitized solar cell by core e shell AuNRs @ SiO_2 in composite photoanode. J Power Sources 2014;272:1100–5.
[96] Xu Q, Liu F, Liu Y, Cui K, Feng X, Zhang W, Huang Y. Broadband light absorption enhancement in dye-sensitized solar cells with Au-Ag alloy popcorn nanoparticles. Sci Rep 2013;3:2112.
[97] Wang D, Li Y. Bimetallic nanocrystals: liquid-phase synthesis and catalytic applications. Adv Mater 2011;23:1044–60.
[98] Rycenga M, Xia X, Moran CH, Zhou F, Qin D, Li ZY, Xia Y. Generation of hot spots with silver nanocubes for single-molecule detection by surface-enhanced Raman Scattering. Angew Chemie Int Ed 2011;50:5473–7.
[99] Haggui M, Dridi M, Plain J, Marguet S, Perez H, Schatz GC, Wiederrecht GP, Gray SK, Bachelot R. Spatial confinement of electromagnetic hot and cold spots in gold nanocubes. ACS Nano 2012;6:1299–307.
[100] Sau TK, Murphy CJ. Room temperature, high-yield synthesis of multiple shapes of gold nanoparticles in aqueous solution. J Am Chem Soc 2004;126:8648–9.
[101] Gangishetty MK, Scott RWJ, Kelly TL. Panchromatic enhancement of light-harvesting efficiency in dye- sensitized solar cells using thermally annealed Au@SiO_2 triangular nanoprisms. Langmuir 2014;30:14352–9.
[102] Gangishetty MK, Lee KE, Scott RWJ, Kelly TL. Plasmonic enhancement of dye sensitized solar cells in the red-to-near-infrared region using triangular core shell Ag@SiO_2 nanoparticles. ACS Appl Mater Interfaces 2013;5:11044–51.
[103] Elbohy H, Kim MR, Dubey A, Reza KM, Ma D, Zai J, Qian X, Qiao Q. Incorporation of plasmonic Au nanostars into photoanode for higher efficiency dye-sensitized solar cells. J Mater Chem A 2016;4:545–51.
[104] Swierk JR, Mallouk TE. Design and development of photoanodes for water-splitting dye-sensitized photoelectrochemical cells. Chem Soc Rev 2013;2357–87.
[105] Emin S, Singh SP, Han L, Satoh N, Islam A. Colloidal quantum dot solar cells. Sol Energy 2011;85:1264–82.
[106] Kamat PV. Boosting the efficiency of quantum dot sensitized solar cells through modulation of interfacial charge transfer. Acc Chem Res 2012;45:1906–15.
[107] Sambur JB, Novet T, Parkinson BA. Multiple exciton collection in a sensitized photovoltaic system. Science 2010;330:63–6.
[108] Stenzel O, Stendal A, Voigtsberger K, von Borczyskowski C. Enhancement of the photovoltaic conversion efficiency of copper phthalocyanine thin film devices by incorporation of metal clusters. Sol Energy Mater Sol Cells 1995;37:337–48.
[109] Stuart HR, Hall DG. Island size effects in nanoparticle-enhanced photodetectors. Appl Phys Lett 1998;73:3815–7.
[110] Kawawaki T, Wang H, Kubo T, Saito K, Nakazaki J, Segawa H. Efficiency enhancement of PbS quantum Dot/ZnO nanowire bulk-heterojunction solar cells by plasmonic silver nanocubes. ACS Nano 2015;9:4165–72.
[111] Paz-Soldan D, Lee A, Thon SM, Adachi MM, Dong H, Maraghechi P, Yuan M, Labelle AJ, Hoogland S, Liu K, Kumacheva E, Sargent EH. Jointly tuned plasmonic-excitonic photovoltaics using nanoshells. Nano Letters 2013;13: 1502–8.
[112] Burschka J, Pellet N, Moon S-J, Humphry-Baker R, Gao P, Nazeeruddin MK, Grätzel M. Sequential deposition as a route to high-performance perovskite-sensitized solar cells. Nature 2013;499:316–9.
[113] Kojima A, Teshima K, Shirai Y, Miyasaka T. Organometal halide perovskites as visible-light sensitizers for photovoltaic cells. J Am Chem Soc 2009;131:6050–1.
[114] Liu M, Johnston MB, Snaith HJ. Efficient planar heterojunction perovskite solar cells by vapour deposition. Nature 2013;501:395–8.
[115] Available at: http://www.nrel.gov/ncpv/images/efficiency_chart.jpg. Accessed on March 2016.

[116] Snaith HJ. Perovskites: the emergence of a new era for low-cost, high-efficiency solar cells. J Phys Chem Lett 2013;4:3623–30.
[117] Zhang W, Saliba M, Stranks SD, Sun Y, Shi X, Wiesner U, Snaith HJ. Enhancement of perovskite-based solar cells employing core-shell metal nanoparticles. Nano Lett 2013;13:4505–10.
[118] Lu Z, Pan X, Ma Y, Li Y, Zheng L, Zhang D, Xu Q, Chen Z, Wang S, Qu B, Liu F, Huang Y, Xiao L, Gong Q. Plasmonic-enhanced perovskite solar cells using alloy popcorn nanoparticles. J Mater Chem 2014;2:11175–9.
[119] Hsu H-L, Juang T-Y, Chen C-P, Hsieh CM, Yang CC, Huang CL, Jeng RJ. Enhanced efficiency of organic and perovskite photovoltaics from shape-dependent broadband plasmonic effects of silver nanoplates. Sol Energy Mater Sol Cells 2015;140:224–31.
[120] Saliba M, Zhang W, Burlakov VM, Stranks SD, Sun Y, Ball JM, Johnston MB, Goriely A, Wiesner U, Snaith HJ. Plasmonic-induced photon recycling in metal halide perovskite solar cells. Adv Funct Mater 2015;25:5038–46.
[121] Even J, Pedesseau L, Katan C. Analysis of multivalley and multibandgap absorption and enhancement of free carriers related to exciton screening in hybrid perovskites. J Phys Chem C 2014;118:11566–72.
[122] Lin Q, Armin A, Chandra R, Nagiri R, Burn PL, Meredith P. Electro-optics of perovskite solar cells. Nat Photonics 2014;9:106–12.
[123] Carretero-Palacios S, Calvo M E, Míguez H. Absorption enhancement in organic–inorganic halide perovskite films with embedded plasmonic gold nanoparticles. J Phys Chem C 2015;119:18635–40.